Methane retrieval from airborne HySpex observations in the short-wave infrared

Philipp Hochstaffl[1], Franz Schreier[1], Claas Henning Köhler[1], Andreas Baumgartner[1], and Daniele Cerra[1]
[1]Deutsches Zentrum für Luft- und Raumfahrt, Institut für Methodik der Fernerkundung, 82234 Oberpfaffenhofen, Germany
Correspondence: Philipp Hochstaffl (philipp.hochstaffl@dlr.de)

Abstract. A reduction of methane emissions could help mitigate global warming on a short time scale, making monitoring of local and regional anthropogenic methane emissions crucial for understanding the methane budget. The study compares various retrieval schemes for estimating localized methane enhancements around ventilation shafts in the Upper Silesian Coal Basin in Poland, using nadir observations in the short-wave infrared from the airborne imaging spectrometer HySpex. Nonlinear and linear methods are examined and put into perspective, with an emphasis on strategies to address degeneracies between the surface reflectivity and the broad band molecular absorption features attributed to the instrument's low spectral resolution. The results demonstrate that the weighted nonlinear least squares fit in the Beer InfraRed Retrieval Algorithm (BIRRA), where the scene's background covariance structure accounts for the reflectivity statistics, is able to quantify enhanced methane levels from hyperspectral data with good accuracy and precision. Some BIRRA setups suffer from surface-type dependent biases although combining multiple spectral intervals mitigates the adverse impact. Linear estimators such as the Matched Filter (MF) and the Singular Value Decomposition (SVD) are fast and able to detect and to a certain extend quantify enhanced levels of methane. Using k-means clustering in a preprocessing step can further enhance the performance of the two linear solvers. The linearized BIRRA fit (LLS) underestimates methane but agrees well on the enhancement pattern. The non-quantitative Spectral Signature Detection (SSD) method does not require any forward modeling and can be useful in the detection of relevant scenes. In conclusion, the BIRRA code — originally designed for the retrieval of atmospheric constituents from space borne high resolution spectra, turned out to be applicable to hyperspectral imaging data for the quantification of methane plumes from point-like sources. Moreover, it is able to outperform well established linear schemes such as the MF or SVD, however, at the expense of high(er) computing time.

1 Introduction

Methane (CH_4) is the second most important anthropogenic greenhouse gas next to carbon dioxide (CO_2) according to the latest IPCC report (Masson-Delmotte et al., 2021). Due to its comparatively short lifetime of approximately 9 years, a reduction of methane emissions could help to mitigate global warming on a relatively short time scale of approximately one decade. Despite improvements in monitoring regional and global CH_4 emissions in recent years the IPCC report points out that fundamental uncertainties pertaining to the methane budget remain (Intergovernmental Panel on Climate Change, 2014).

Observations indicate an increasing trend in atmospheric CH_4 content since 2007, the cause of which is still subject to scientific debate. The vast majority of anthropogenic CH_4 emissions is caused by small scale phenomena such as agriculture (enteric fermentation & manure), waste management (landfills) and fossil fuel exploitation, where the latter is responsible for 20-30 % of all anthropogenic CH_4 emissions. Consequently there exists the need for continuous long-term methane observations on a global scale, in order to foster understanding on the global methane cycle, devise future reduction measures and monitor their effectiveness. The monitoring of anthropogenic emissions of CH_4 and CO_2 is also part of the United Nations Framework Convention on Climate (2015) as nationally determined contributions should be assessed via global stock takes on a 5 year basis from 2023 (Article 13 & 14 of the Paris Agreement).

Satellite observations are typically the method of choice for such continuous and global long-term observations although also ground based networks such as the Global Atmosphere Watch (GAW) Programme of the World Meteorological Organisation (WMO) or the European Integrated Carbon Observation System (ICOS) are crucial assets in monitoring atmospheric composition. Space-borne spectrometers measuring short-wave infrared (SWIR) solar radiation reflected at the Earth surface are especially well-suited to observe atmospheric CH_4 in the lower atmosphere by measuring its absorption around 1.6 μm and and 2.3 μm. In contrast, the thermal infrared is less sensitive to variations in CH_4 concentration close to the surface. Moreover, mid-infrared sensors often have lower spatial resolution making them less favorable for emission monitoring (Richter, 2010).

Operational CH_4 products from contemporary atmospheric composition missions such as TROPOMI (TROPOspheric Monitoring Instrument; Veefkind et al. (2012)), GOSAT/GOSAT-2 (Greenhouse gases Observing SATellite; Kuze et al. (2009, 2016)) measure trace gas concentrations with very high accuracy, nevertheless, they are not optimally suited to measure emissions of point-like sources. This design inherent limitation is due to their focus on rapid global coverage, which entails a comparatively coarse spatial resolution of several square kilometers per pixel. Since the emission of a single point source inside a pixel is averaged over the entire resolution cell, even large sources seldomly elevate the mean CH_4 concentration within one pixel by more than one percent compared to the undisturbed background (Lauvaux et al., 2022). A way to increase the contrast of enhancements is to operate typical atmospheric remote sensing spectrometers at lower altitudes (e.g. on aircraft), thus increasing the spatial resolution while leaving the overall optical design untouched. This strategy is followed by instruments such as MAMAP/MAMAP-2D (Gerilowski et al., 2011) or GHOST (Humpage et al., 2018) which are very well-suited for the calibration and validation of their space-borne counterparts.

In order to increase the sensitivity towards smaller sources an increased spatial resolution is required. This in turn necessitates a trade-off in spectral resolution because the loss of photons caused by the smaller ground pixels reduces the Signal-to-Noise Ratio (SNR) of the image which has to be compensated by broadening the spectral interval per spectral channel. Imaging spectrometers for land surface remote sensing (often referred to as hyperspectral cameras) are typical examples of instruments optimized for spatial resolution this way. Their technology matured over the last 30 years and a variety of airborne instruments and several space-borne versions are either in orbit Guanter et al. (2021, PRISMA), Chabrillat et al. (2020, ENMAP) or going to be launched in the future Rast et al. (2021, CHIME). Yet other sensors dedicated for the detection of methane Jervis et al. (2021, GHGSat) or MethaneSat and carbon dioxide, e. g., Hochstaffl et al. (2023, CO2Image), have slightly higher spectral

resolution than their hyperspectral counterparts but still offer a much higher spatial resolution than atmospheric composition missions.

Thorpe et al. (2013) were the first to demonstrate that localized CH_4 emissions over land can be detected from hyperspectral cameras with the Airborne Visible/Infrared Imaging Spectrometer Green et al. (1998, AVIRIS) and that a limited quantitative analysis is possible (Thorpe et al., 2014). Similar studies were repeated with airborne instruments (AVIRIS-NG, Frankenberg et al. 2016; Duren et al. 2019; Borchardt et al. 2021; HySpex, Nesme et al. 2020) and space-borne instruments (Thompson et al., 2016; Guanter et al., 2021). Varon et al. (2019) and Jervis et al. (2021) demonstrated that CH_4 sources can even be detected with the multi-spectral MSI instrument on-board the Sentinel-2 satellites, but these measurements are restricted to 'favourable conditions' (i. e., strong sources and high surface albedo).

One of the core challenges when retrieving methane from measurements with high spatial and moderate spectral resolution (> 1 nm) is the separation of spectral variations caused by molecular absorption and surface reflectivity (Ayasse et al., 2018). Classical trace gas retrievals for high-spectral resolution instruments such as RemoteC (Lorente et al., 2021), Weighting Function Modified Differential Optical Absorption Spectroscopy (Buchwitz et al., 2005, WFM-DOAS), or the Beer InfraRed Retrieval Algorithm (Gimeno García et al., 2011, BIRRA) exploit the high frequency characteristics of gaseous absorption and attribute the smooth varying part to the surface albedo and scattering. Instruments with coarse spectral resolution, however, are unable to sufficiently resolve those molecular signatures which causes ambiguities that often leads to surface-type related biases in the 'classical' retrieval schemes (e. g., Borchardt et al. (2021, Sec. 3.3) or Thorpe et al. (2014, Sec. 9.2)). Alternative more 'data-driven' retrieval schemes such as the Matched Filter (MF) or the Singular Value Decomposition (SVD) estimate enhancements based on methods from linear algebra and statistics (Thorpe et al., 2013; Thompson et al., 2015; Thorpe et al., 2014).

This study aims to compare various retrieval schemes applied to measurements from the German Aerospace Center's (DLR) HySpex sensor system. The objective is to evaluate the retrievals performance in terms of accuracy, precision and speed and show advantages and drawbacks for each method. Another goal is to assess the latest BIRRA updates and its applicability to moderately resolved spectra from airborne sensors. Therefore, the paper is structured as follows: First, the experimental setup is briefly described, followed by a quick review of atmospheric radiation and an introduction to the various BIRRA setups examined in this study. Afterward, other simpler but faster retrieval schemes employed in this work are briefly discussed. The result section starts with a feasibility analysis and then proceeds with the presentation of the retrieval results from HySpex observations over the Pniowek V ventilation shafts. In the last section, the results are summarized and put into perspective.

2 Methodology

The methodology introduced in this section can be divided into linear and nonlinear schemes. While the former are very fast and often of sufficient accuracy, the nonlinear iterative solvers require more computing power and time to come up with a best estimate. The retrieval methods are tailored to address the issue of albedo-related biases, which arises due to correlations with broad-band absorption features resulting from the instrument's low spectral resolution.

The data analyzed in this study was collected with the DLR HySpex sensor system during a survey flight conducted within the scope of the COMET (Carbon diOxide and METhane) campaign on June 7th, 2018. The CoMet campaign focused on the detection and characterization of CO_2 and CH_4 sources in the Upper Silesian Coal Basin (USCB) in southern Poland.

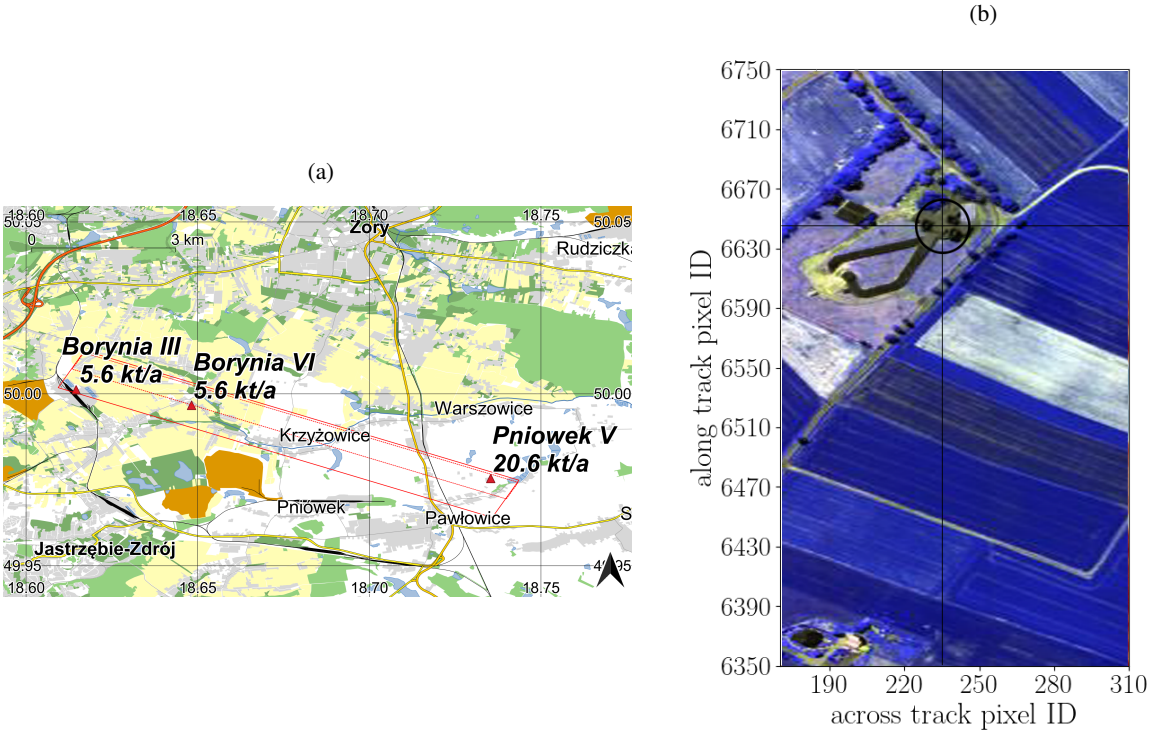

Figure 1. (a) Flight lines 09 and 11 are illustrated as a dashed red line and a solid red line, respectively. Flight line 9 was obtained around 09:55 UTC, while Flight line 11 was acquired around 10:10 UTC. The aircraft flew at an altitude of approximately ≈ 1.200 m and ≈ 2.600 m above ground level, respectively, while heading eastward at 115 degrees. The map was generated using QGIS software and OpenStreetMap data (OpenStreetMap contributors, 2022). **(b)** False color image from the SWIR-320m-e camera around the three Pniovek V shafts in scene 09.

The airborne imaging spectrometer HySpex consists of two commercially available hyperspectral cameras (a VNIR-1600 and a SWIR-320m-e) and its basic specifications are presented in Table 1. The aim of this survey was to conduct evaluate the feasibility of localized methane emission retrieval using the SWIR-320m-e data. To achieve this goal we planned 18 flight lines at two different altitudes over a number of known ventilation shafts around Katowice. However, it was not known in advance which of these ventilation shafts would be actively emitting methane during overpass, because only monthly averages of the emission rates are reported by the mining companies operating the shafts Nickl et al. (2020).

Table 1. Summary of some important HySpex properties. The sensor is described in detail in (IMF) and references therein.

HySpex specifications	
Detector	MCT Sofradir MARS
Spectral Range [nm]	968-2498
Field of View (with FoV Expander) [°]	13.2 / 27.2
Number of (spectral) Channels	256
Sampling Interval [nm]	6.0
Bandwidth [nm]	5.6–7.0
Number of (geometric) Pixels	320
Dynamic Range [bit]	14

The weather during the survey was well-suited for remote sensing measurements. Apart from very few occasional patches of thin cirrus clouds there were no further low or mid-infrared-level clouds. However, some amount of haze was observed from the aircraft during the flights. Actual wind data for the USCB area on the measurement day is presented in Luther et al. (2022, Fig. 4 and 6). Fig. 1 displays the flight tracks over the Pniovek V and other two shafts. It took the aircraft approximately three
105 minutes to complete one track, during which time 7130 (scene 09) and 5075 (scene 11) observations were recorded for each of the 320 across-track detector pixels. To compare the effectiveness of various retrieval methods, we limit our analysis to the two flight lines shown in Fig. 1a, namely Flight line 9 (called scene 09) and Flight line 11 (called scene 11). The map also depicts the location of the potential sources with their nominal (reported) emission rates.

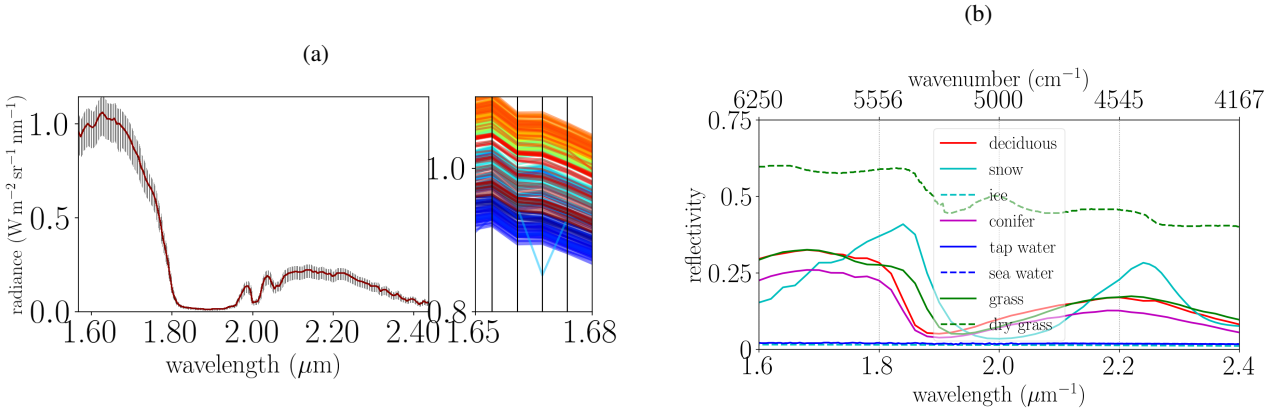

Figure 2. (a) HySpex average spectrum with the span (minimum to maximum) depicted in gray for measurements across the 320 across track detector pixels for scene 09 (left). The center shows a bunch of individual spectra around 1.67 μm with the black lines indicating the pixel positions and sampling distance. The radiance values of pixel 104 (cyan) at ≈ 1.677 μm (5960 cm^{-1}), which is relevant for the CH4 retrieval appears to be problematic. **(b)** Reference reflectances for different surface types (measured at the John Hopkins University).

In Fig. 2a an ensemble of along track averaged HySpex measurements is depicted. The sensor's sampling distance across the spectral axis is indicated by the vertical grid lines. The spectral coverage of the HySpex SWIR-320m-e camera ranges from 967–2496 nm (4005–10338 cm^{-1}), with the exact number depending on the across track pixel ($\approx \pm 1\ \mathrm{cm}^{-1}$). The figure shows that the radiative intensity in the interval around 1.6 μm ($\approx$ 6000 cm^{-1}) is significantly larger than that between 2.3 μm ($\approx$ 4300 cm^{-1}) mostly due to $\mathrm{H_2O}$ absorption.

The values for the spectral resolution, i. e., the full width at half maximum (FWHM) of the SWIR-320m-e camera in the 1500–2500 nm (4000–6500 cm^{-1}) region ranges from 6.0–9.5 nm (10–40 cm^{-1}), are provided for each across track pixel of the detector (a 2D array) with the level 1b data set. This data set was basically created as described in Lenhard et al. (2015), except for the optical distortion correction. The Instrument Spectral Response Function (ISRF) calibration was performed according to Baumgartner (2021). Hence, the ISRF for each pixel is available as a lookup table with an sampling distance of 1.2 nm.

Figure 2b displays reference reflectances for various surface types across the same spectral interval. Due to the instrument's coarse spectral resolution, the measurement is only capable of resolving broad-band molecular absorption features. A possible bad pixel is shown in the figure around 1.65 nm (a descending cyan line) which shows with systematically lower radiance values along the flight track. The pixel corresponding to across track pixel 104.

2.1 Radiative transfer

In the SWIR spectral range the radiative transfer through the atmosphere under clear sky conditions (cloud and scattering free in general) is well described by Beer's law (Zdunkowski et al., 2007) with the monochromatic transmission in wavenumbers ν given by

$$\mathcal{T}_m(\nu; s) \;=\; \exp\left(-\sum_m \tau_m(\nu, s)\right) \;=\; \exp\left(-\int_{\mathrm{path}} \mathrm{d}s \sum_m n_m(s)\, k_m\big(\nu, p(s), T(s)\big)\right). \tag{1}$$

The model assumes a pure gas atmosphere with molecular m optical depth τ given by the path integral along s over the molecular number densities n_m and k_m, the pressure p and temperature T dependent absorption cross section. This study utilizes the 2020 spectroscopic line data from GEISA (Gestion et Etude des Informations Spectroscopiques Atmosph'eriques; Delahaye et al., 2021) for molecular absorption calculations.

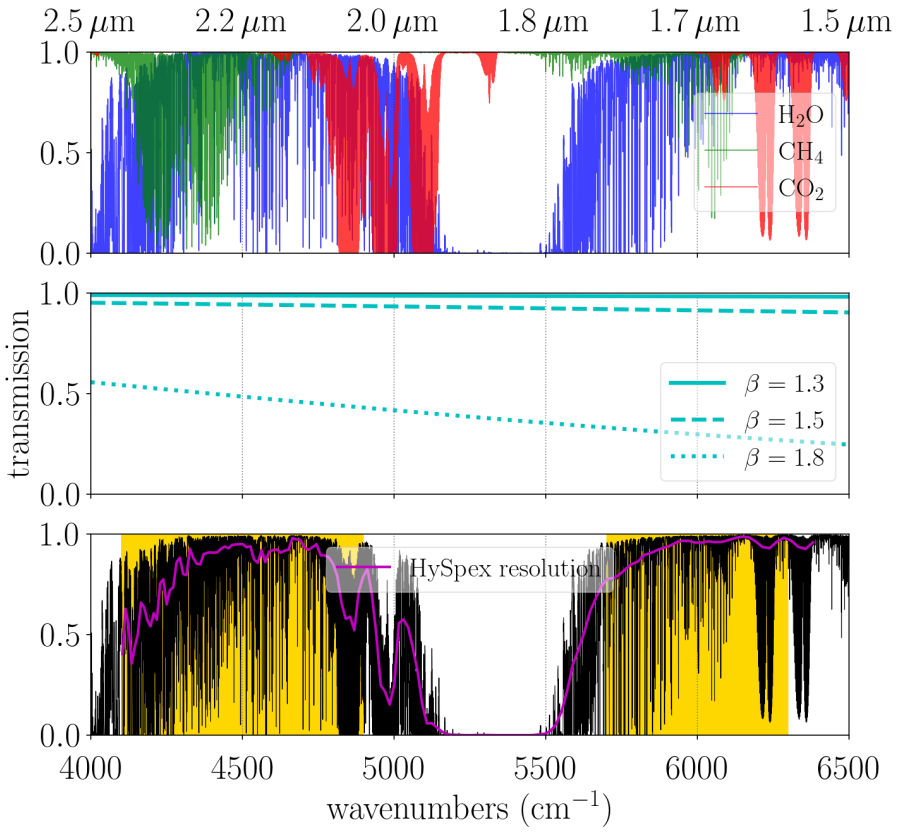

Figure 3. Monochromatic transmissions of CH_4, CO_2 and H_2O for the SWIR spectral range and a nadir looking observer at 1.5 km at a solar zenith angle (SZA) of 30° are depicted in the top panel. The aerosol transmission in the mid-infrareddle panel has only smooth variations across the spectrum. The magenta line in the lower panel represents the total transmission degraded to HySpex resolution. The spectral intervals used for the CH_4 fit are indicated by the yellow background. The two fitting windows range from 4100–4900 cm^{-1} (4K) and 5700–6300 cm^{-1} (6K), respectively. Note significant differences in transmissions of the monochromatic spectrum and convolved instrument spectrum.

In conditions where particles such as haze, dust or high clouds prevail, extinction (scattering and absorption) by aerosols should be taken into account (De Leeuw et al., 2011). Aerosol optical thickness is often described by a simple power law with an exponent β (details see Hochstaffl (2022)). The mid-infrareddle panel in Fig. 3 exemplary depicts such a model's result for different exponents.

In Fig. 3, the top panel shows the individual components of the monochromatic total transmission for the US-Standard atmosphere, including methane's first overtone of the fundamental vibrational transition $2\nu_3$ (with its P and R branches) around 6000 cm^{-1} (1560-1660nm, tetradecad band), as well as additional strong absorption lines ranging from 4200–4600 cm^{-1} (2090-2290nm, octad). The bottom panel illustrates how the observer's coarse spectral resolution smooths the total monochro-

matic transmission (shown in black). There are 67 and 28 HySpex pixels used by the retrievals within the range of the 4K and 6k spectral windows, respectively.

2.2 Model atmosphere setup

The model atmosphere's vertical extent ranges from 0–80 km with 39 levels in total. The atmosphere is composed of pure gaseous layers above altitude $z = 10\,\mathrm{km}$ and layers containing gases and particles below $z = 10\,\mathrm{km}$. The vertical resolution is highest in the (plume) layer below $z_{\mathrm{pl}} = 2\,\mathrm{km}$ where the enhancement is expected to takes place. The $\mathrm{CH_4}$ optical depth is modeled in terms of a climatological background and a Gaussian plume

$$\tau_{\mathrm{CH_4}} \;=\; \tau_{\mathrm{bg}} \;+\; \alpha\,\tau\;, \tag{2}$$

where α represents the molecular scaling factor for the plume optical depth while τ_{bg} represents the background.

Although the shape of the plume profile is not crucial as the nadir viewing geometry does not allow to retrieve information on the vertical distribution of trace gases in the SWIR (see Buchwitz et al., 2000, Sec. 3) our setup constrains the fit to the lowest atmospheric layer up to 2.0 km (see Thorpe et al., 2014, 5.2).

The $\mathrm{CH_4}$ background profile as well as the $\mathrm{CO_2}$ background profile are modeled according to the Air Force Geophysical Laboratory (Anderson et al., 1986, AFGL) atmospheric constituent profiles scaled to 1875 ppb and 400 ppm, respectively. The molecules $\mathrm{H_2O}$ as well as the auxiliary parameters temperature and pressure are taken from reanalysis data provided by the National Center for Environmental Prediction (Kalnay et al., 1996, NCEP).

2.3 Beer InfraRed Retrieval Algorithm (BIRRA)

The *BIRRA level 2 processor*, developed at DLR, uses the line-by-line forward model Generic Atmospheric Radiation Line-by-line InfraRed Code (Schreier et al., 2014, GARLIC) and a separate (SLS) or nonlinear least squares solver (NLS) for trace gas retrieval in the SWIR spectral region (Hochstaffl et al., 2018). It has been successfully applied to SCIAMACHY (Scanning Imaging Absorption Spectrometer for Atmospheric Chartography, Gimeno García et al., 2011; Hochstaffl and Schreier, 2020) and TROPOMI (TROPOspheric Monitoring Instrument, Hochstaffl et al., 2020) observations. In this study, however, the new Python version of BIRRA is used which is based on Py4CAtS (Python for Computational Atmospheric Spectroscopy, (Schreier et al., 2019)), a Python reimplementation of the validated Fortran code GARLIC (Schreier et al., 2013).

The mathematical forward model $\Phi(\boldsymbol{x}, \nu)$ describes the measured intensity spectrum $I(\nu)$ for a nadir looking observer according to

$$\Phi(\boldsymbol{x}, \nu) \;=\; \frac{r(\nu)}{\pi}\,\cos(\theta)\,I_{\mathrm{sun}}(\nu)\,\mathcal{T}_m^{\downarrow}(\nu)\,\mathcal{T}_m^{\uparrow}(\nu) \otimes S(\gamma(\nu))\;, \tag{3}$$

where r refers to the surface reflectivity and θ represents the solar zenith angle. The terms $\mathcal{T}_m^{\downarrow}$ and $\mathcal{T}_m^{\uparrow}$ denote the total transmission between Sun and reflection point (e.g. the Earth) and between reflection point and observer, respectively (see Eq. 1). The transmission by aerosols for different Ångstrom exponents according to is depicted in Fig. 3 (center). Its behavior can be

represented by a low order polynomial hence the forward's model total transmission is described as

$$\mathcal{T}_m(\nu; s) \;=\; \exp\left(-\sum_m \alpha_m\, \tau_m(\nu) - \sum_{i>0} a_i\, \nu^i\right). \tag{4}$$

The unknown (to be estimated) parameters are composed as elements of the state vector $\boldsymbol{x}$ and include the molecular scaling factors α_m, the aerosol coefficients a_i, and the coefficients for the surface reflectivity r_j (with $j \geq 0$) which is also modeled by a polynomial. Note that since the information of the vertical profile is well under-determined in the observed spectrum scaling factors α_m for the initial guess profiles are retrieved (Gimeno García et al., 2011, Fig. 1). Finally, the instrument's spectral response is described by the ISRF S. Its parameters such as the half width γ or a spectral shift can (optionally) be part of the state vector.

2.3.1 Nonlinear solvers

This study examines various nonlinear retrieval schemes that were implemented in the BIRRA level 2 processor and are briefly introduced below. Nonlinear least squares methods are iterative and require calculating derivatives for each of the nonlinear state vector elements across the spectral axis, represented by a Jacobian matrix J. Note that $||\cdot||$ represents the 2-norm throughout this study.

Nonlinear (NLS) and separable least squares (SLS)

The nonlinear least squares fit minimizes the objective function $\mathcal{L}$ for given measurements $\boldsymbol{y}$ according to

$$\min_{\boldsymbol{x}} \|\boldsymbol{y} - \boldsymbol{\Phi}(\boldsymbol{x})\|^2\,, \tag{5}$$

and applies when the model function $\boldsymbol{\Phi}$ is nonlinear in one or more parameters of $\boldsymbol{x}$.

The so called separable least squares solver splits (separates) the state vector $\boldsymbol{x}$ into nonlinear and linear parameters $\boldsymbol{x} = (\boldsymbol{\eta}, \boldsymbol{\zeta})$ where the elements in $\boldsymbol{\zeta}$ enter the forward model $\boldsymbol{\Phi}$ linearly (see Sec. 2.4.1). The minimization problem is hence given by

$$\min_{\eta,\zeta} \|\boldsymbol{y} - \boldsymbol{\Phi}(\boldsymbol{\eta})\, \boldsymbol{\zeta}(\eta)\|^2\,. \tag{6}$$

This setup is also known as the Variable Projection (VarPro, Golub and Pereyra, 2003) method where $\boldsymbol{\eta}$ is independent of $\boldsymbol{\zeta}$ in the matrix product $\boldsymbol{\Phi}(\boldsymbol{\eta})\, \boldsymbol{\zeta}(\boldsymbol{\eta})$. The parameters in $\boldsymbol{\eta}$ can hence be fitted in the usual way by means of Gauss–Newton or Levenberg–Marquardt algorithms (Hansen et al., 2013, see).

Generalized least squares (GLS)

To account for correlated errors, a generalized least squares fit is used. The covariance matrix C takes into account the spectral variations of the scene's background, which includes parts of the flight track that are not affected by the CH_4 plume. To create the matrix C, the location of the point source and wind data must be known. The spectral covariance for a given

scene is computed to account for possible background variations similar to methane band absorption that could be mistakenly interpreted as a molecular enhancement. Fig. 4 shows the covariance matrices for the methane retrieval intervals.

The error covariance matrix C is a symmetric positive semi-definite matrix that is precomputed for each flight track. To account for correlated errors, the non-negative square root matrix $\mathsf{S} = \mathsf{C}^{1/2}$ is used to estimate $\boldsymbol{x}$ by minimizing the 2-norm of the weighted residual vector:

$$\min_{\boldsymbol{x}} ||\mathsf{S}^{-1}(\boldsymbol{y} - \boldsymbol{\Phi}(\boldsymbol{x}))||^2. \tag{7}$$

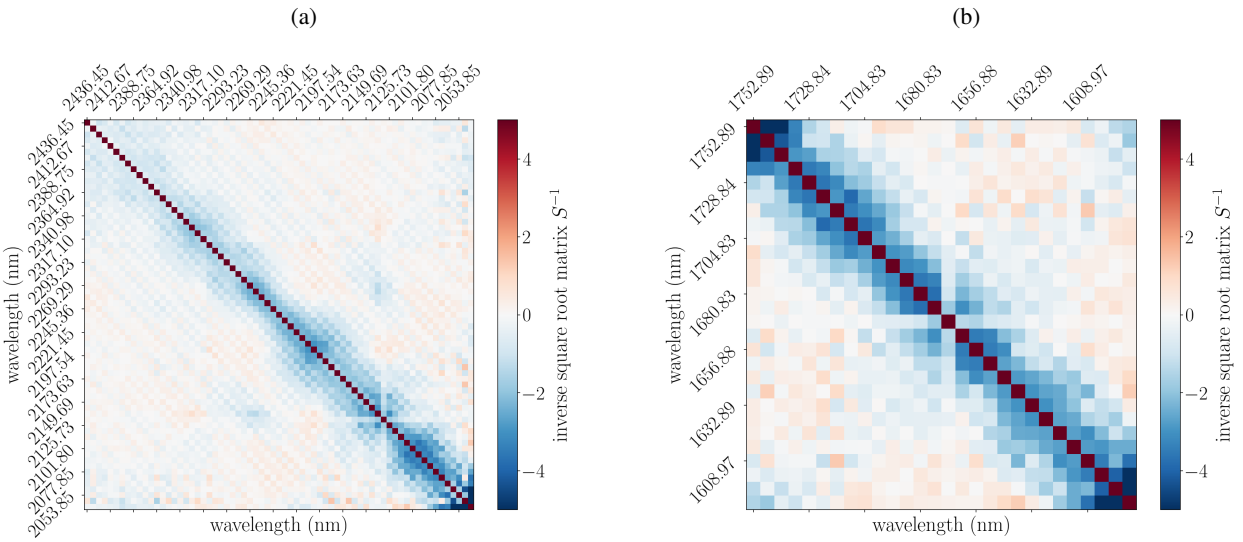

Figure 4. Scene 09 background covariance matrix for the **(a)** 4100-4900 cm^{-1} (4K, left) and **(b)** 5700-6300 cm^{-1} (6K, right) spectral range. The background area was defined outside of the pixels along-track=$(6300, 6670)$, across-track=$(180, 285)$. Note that beside the bad HySpex pixel mentioned in Fig. 2 at 5992.74 cm^{-1} there appears to be another suspect pixel at 4691.04 cm^{-1}.

2.3.2 Methane enhancement estimate for nonlinear solvers

The state vector $\boldsymbol{x}$ for the methane plume fit comprises the CH_4 scaling factor and a second-order reflectivity polynomial per spectral window. Further parameters were found to be unnecessary as they did not improve the retrieval outcome but rather destabilized the solutions, owing to an increase in the condition number of the Jacobi matrix.

A scene averaged spectrum, excluding ground pixels around the suspected CH_4 sources, was employed to estimate H_2O, CO_2 and CH_4 background concentrations. The CO_2 background level of the scene is inferred from the 1.6 μm and 2 μm bands via a multi-interval (4K and 6K spectral windows) fit. A scene averaged background scaling factor of $\tilde{\alpha}_{CO2} = 0.96$ for scene 09 and $\tilde{\alpha}_{CO2} = 0.93$ for scene 11 was found. Due to the degeneracy between H_2O and the reflectivity polynomial at HySpex's spectral resolution the scene averaged H_2O scaling factor should be viewed as effective parameter that partly captures low frequency components in the spectrum. The scene averaged CH_4 background profile was found to be within 5 % of the initial guess of 1875 ppbv, hence it was maintained and not scaled.

The decision to exclude aerosol parameters from the CH_4 plume fit was encouraged by findings from Borchardt et al. (2021), who concluded that different aerosol scenarios in the SWIR do not induce errors greater than 0.2 %. Moreover, since the spectra were observed at low flight altitudes on a rather clear day (see Fig. 1 and Luther et al. 2019), retrieval errors induced by aerosol scattering should be negligible in our scenario as well (also see Fig. 3 and Thorpe et al. 2013; Thompson et al. 2015). Nonetheless the study accounts for light path modifications in the reported CH_4 estimates by using the scene average α_{CO2} scaling factor from above. The actual CH_4 column given by the background concentration plus the retrieved enhancement includes corrections for light path modifications via the prefitted scene averaged background CO_2 $\tilde{\alpha}_{CO2}$ given by

$$N_{CH4} = N_{bg} + \frac{\alpha}{\tilde{\alpha}_{CO2}} \hat{N}_{pl}(z_0) , \tag{8}$$

with

$$\hat{N}_{pl}(z_0) = \int_{z_0}^{z_{pl}} n_{pl}(z)\,dz , \tag{9}$$

and z_0 representing the bottom of the atmosphere. Note that this approach assumes that the CO_2 profile upon which $\tilde{\alpha}_{CO2}$ was estimated corresponds to the true profile and that $\tilde{\alpha}_{CO2}$ is 1 in absence of scattering. The actual retrieval fits the methane enhancement factor along with a second order reflectivity polynomial so that the state vector is given by $\boldsymbol{x} = (\alpha, r_0, r_1, r_2)$. This setup is found robust toward lower SNR values and less prone to correlations across state variables.

2.4 Linear solvers

In contrast to nonlinear fitting schemes, linear solvers for $\boldsymbol{x}$ can only be used when equations can be expressed as a linear combination of the variables in $\boldsymbol{x}$. To utilize such methods, it is usually required to linearize the forward model with respect to the variables of interest. The solvers can be split into two groups, i. e., one that take background statistics into account (MF and SVD) and the two others that do not (LLS and SSD).

2.4.1 Linear least squares (LLS)

The LLS method uses a linear fitting scheme to estimate the CH_4 parameter (see Eq. 2). Assuming that the increase in optical depth caused by the plume, τ, is relatively small, the BIRRA forward model from Sec. 2.3 is linearized with respect to α by approximating the transmission spectrum of the plume by Taylor expansion according to

$$\exp(-\tau) \approx (1 - \alpha\,\tau) . \tag{10}$$

The linear least squares problem of M measurements can then be formulated according to

$$\min_{\boldsymbol{x}} ||\boldsymbol{y} - \boldsymbol{\Phi}\,\boldsymbol{x}|| \tag{11}$$

where the model functions in $\boldsymbol{\Phi}$ for the linear parameters of the state vector $\boldsymbol{x} = (r_0, b_0 = r_0\,\alpha)$ are given by

$$\phi_1 = \frac{\cos(\theta)}{\pi} I_{sun}\,\mathcal{T}^{\downarrow}\mathcal{T}^{\uparrow} \otimes S, \tag{12}$$

$$\phi_2 = -\frac{\cos(\theta)}{\pi} I_{sun}\,\mathcal{T}^{\downarrow}\mathcal{T}^{\uparrow}\,\tau \otimes S. \tag{13}$$

It is important to note that with this setup the reflectivity coefficient r_0 is present in both elements of the state vector. In order to avoid this and allow for higher order reflectivity polynomials in the fit, which are required for large spectral intervals, the retrieval is performed in two steps. In a first step only the reflectivity coefficients are fitted while in a second step α is estimated with the prefitted reflectivity coefficients given as input. This setup allows fits for an increased spectral interval. In addition, the setup allows for spectral separation by de-weighting individual pixels in the albedo fit that are impacted by methane. This basically ensures that the reflectivity coefficients can be fitted outside the absorption bands of the target, and then the enhancement factor can subsequently be estimated from the range where absorption occurs. This approach minimizes interference between the two fits, preventing the reflectivity polynomial from capturing absorption of $\mathrm{CH_4}$.

Another aspect that should be kept in mind is that that since $1 - \alpha\tau \leq \exp(-\alpha\tau)$ for $\alpha \geq 0$ the linearized model underestimates the $\mathrm{CH_4}$ enhancement for a given optical depth τ compared to the nonlinear setup (forward plus inversion). However, the setup should be sensitive enough to yield elevated methane levels.

2.4.2 Matched Filter (MF)

The MF is a well-established method for estimating molecular concentration enhancements from hyperspectral sensors, with numerous studies supporting its effectiveness (Theiler and Foy, 2006; Villeneuve et al., 1999; Funk et al., 2001; Thorpe et al., 2013; Thompson et al., 2015). The linear enhancement factor estimate is derived by perturbing an average (background) radiance spectrum $\boldsymbol{\mu}$ with a known target spectrum $\mathbf{t}$. The approach is analogous to that used by Thompson et al. (2015), where $\mathrm{CH_4}$ enhancements are estimated by linearly scaling a target signature that perturbs the mean radiance

$$\alpha_i(\boldsymbol{y}) \;=\; \frac{(\mathbf{t}(\boldsymbol{\mu}))^{\mathrm{T}}\,\mathsf{C}^{-1}\,(\boldsymbol{y}_i - \boldsymbol{\mu})}{\sqrt{(\mathbf{t}(\boldsymbol{\mu}))^{\mathrm{T}}\,\mathsf{C}^{-1}\,(\mathbf{t}(\boldsymbol{\mu}))}}\,. \tag{14}$$

This equation constitutes the linear minimizer that solves the Gaussian log-likelyhood

$$\min_{\alpha_i} ||\mathsf{C}^{-1/2}\boldsymbol{d}||^2 \quad \text{with} \quad \boldsymbol{d} \;=\; \boldsymbol{y}_i - (\boldsymbol{\mu} + \alpha_i\,\mathbf{t}(\boldsymbol{\mu})) \quad \text{and} \quad \mathbf{t}(\boldsymbol{\mu}) \;=\; -\boldsymbol{\mu}\boldsymbol{\tau}\,. \tag{15}$$

The method assumes that the measured spectrum can be represented as a linear superposition of the $\mathrm{CH_4}$ plume's optical depth and the mean unperturbed radiance $\boldsymbol{\mu}$ and tests an observed vector $\boldsymbol{y}_i$ against a base vector while accounting for the background covariance C. Note that the mean background spectrum $\boldsymbol{\mu}$ and C were computed per scene and the inverse covariance C^{-1} is approximated by decomposing C into eigenvalues and eigenvectors (Thompson et al., 2015, Eq. 6-8).

In order to get a more accurate target spectrum estimate, a per pixel estimate of the target spectrum was computed which accounts for the pixel's albedo (Foote et al., 2020, II. Methods, C.). This albedo normalized matched filter includes an albedo factor r_i for each measurement spectrum according to

$$\boldsymbol{d}_{\mathbf{r}} \;=\; \boldsymbol{y}_i - (\boldsymbol{\mu} + r_i\,\alpha_i\,\mathbf{t}(\boldsymbol{\mu})) \quad \text{with} \quad r_i = \frac{\boldsymbol{y}_i^{\mathrm{T}}\,\boldsymbol{\mu}}{\boldsymbol{\mu}^{\mathrm{T}}\,\boldsymbol{\mu}} \tag{16}$$

According to Guanter et al. (2021), the classical matched filter is relatively sensitive to surface albedo which could be mitigated by k-means clustering of the scene. This approach reduces within-class variance, which in turn should minimize the albedo sensitivity of α. In the so called cluster-tuned matched filter, instead of computing a single background covariance

statistic, a background statistic C_i is computed for each cluster i, determined by k-means clustering (Thorpe et al., 2013; Nesme et al., 2020).

2.4.3 Singular Value Decomposition (SVD)

The retrieval of methane enhancements from hyperspectral AVIRIS data using singular vectors of the observed spectrum plus a target signature was first demonstrated by Thorpe et al. (2014). The SVD method is well-suited for parameter estimation from moderately resolved spectral data because it allows to consider only the most significant components of the spectrum while preserving the main spectral information.

In this study the orthogonal singular vectors are obtained from HySpex spectra that are not impacted by the plume. The scene's log-space background spectra I_{bg} was decomposed into $\mathsf{USV}^{\mathrm{T}}$. The target spectrum is represented by the CH_4 plume's optical depth $\boldsymbol{\tau}$ which was computed with Py4CAtS.

The basic idea is analogous to the MF, i. e., to represent the general variability in spectral radiance by a linear combination of singular vectors and a target signal. The minimization problem is then given by

$$\min_{\boldsymbol{w}} ||\boldsymbol{y} - \mathsf{A}\,\boldsymbol{w}||^2 \quad \text{with} \quad \mathsf{A}\,\boldsymbol{w} = \sum_{k}^{N} \boldsymbol{u}_k\, \boldsymbol{w}_k + \boldsymbol{t}\, \boldsymbol{w}_{\mathrm{CH4}} \tag{17}$$

where A represents the concatenated matrix of the first N columns of the unitary matrix U. The vector $\boldsymbol{w}$ contains the corresponding weights with $\alpha = \boldsymbol{w}_{\mathrm{CH4}}$ scaling the contribution of enhanced methane in the lowest atmospheric layers $\boldsymbol{t} = \boldsymbol{\tau}$. In the cluster-tuned variant the background spectra are clustered by k-means and the SVD performed for each cluster separately and the respective base vectors per cluster were then used in the linear fit.

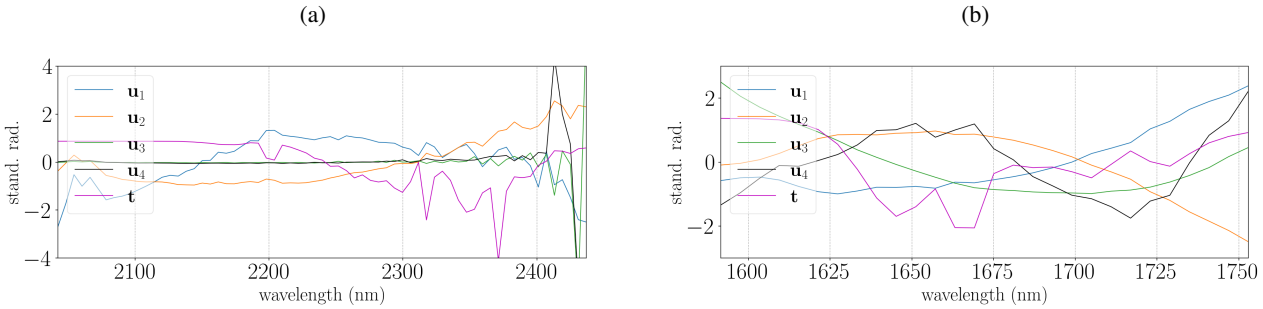

Figure 5. Standardized singular vectors and the methane plume's target signature $\mathbf{t}$ in 4K (left) and 6K (right) spectral intervals, respectively. Standardization removes the mean and scales to unit variance. While the $\boldsymbol{u}$ vectors were yielded from the SVD the vector $\mathbf{t}$ was computed with the radiative transfer model Py4CAtS. Modelling the plume's optical depth with the same tools and for an equivalent setup (< 2 km) is crucial for comparability with the nonlinear BIRRA setups.

2.4.4 Spectral signature detection (SSD)

A straightforward approach for detecting spectral methane absorption is the SSD fit which compares the ratio of spectral residual norms to produce a score. Unlike other methods, this approach does not require any radiative transfer calculations, look-up tables, or initial guess information, only calibrated sensor data for a specific interval.

The algorithm is based on a simple polynomial fit of spectral pixels and the calculation of spectral residuals. The idea behind this method is similar to the continuum interpolated band ratio (CIBR) from Green et al. (1989) and Thompson et al. (2015, Eq. 2), which also measure absorption depths (Pandya et al., 2021). The method splits the spectral interval into pixels where $\mathrm{CH_4}$ absorbs and where it does not (or only weakly, also see the LLS method) and by linear least squares a polynomial of degree P is fitted to the M out-of-band pixels

$$\min_{\boldsymbol{x}} ||\boldsymbol{y} - \boldsymbol{p}(\boldsymbol{x})||^2 \quad \text{with} \quad p(\boldsymbol{x}, \nu_i) \;=\; \sum_{j=0}^{P} \alpha_j \, \nu_i^j \,, \qquad j = 1, 2, \cdots, P \quad \text{and} \quad i = 1, 2, \cdots, M. \tag{18}$$

Next the residual norms for the in- and out-of-band pixels are computed and the ratio formed $r_{\mathrm{in}}/r_{\mathrm{out}}$ which provides an absorption band depth score for each observation, i. e., the score indicates variations in the $\mathrm{CH_4}$ absorption if in- and out-of-band pixels were properly chosen.

The algorithm constitutes a fast detection scheme which can also be applied for real-time detection of enhancements, e. g., determine whether or not a $\mathrm{CH_4}$ ventilation shaft is active at the time of instrument overpass. When a zero order polynomial is used for the out-band fit, the method is comparable to the CIBR algorithm. However, by using higher order polynomials, the method can model the surface reflectivity and other interfering species more precisely, especially over larger spectral intervals.

3 Results

This section presents the results for the $\mathrm{CH_4}$ estimates from various retrieval methods over the Pniovek V shafts. The site was selected since it showed significant methane releases during the times of overpass in flight track 9 (scene 09) and flight track 11 on June 07, 2018 (see Fig. 1). The results presented subsequently focus on measurements from scene 9. Except otherwise stated, the retrievals were performed on 3×3 pixels averaged spectra in order to increase the signal-to-noise ratio and thereby reduce scattering of the $\mathrm{CH_4}$ fits across pixels.

3.1 NLS and SLS fits

Figures 6b and 6c show the results of the classical BIRRA NLS fit. The position of the source is indicated by the intersection of the dashed line. The fits reveals a significant enhancement of $\mathrm{CH_4}$ in both spectral intervals above and downwind of the ventilation shaft. However, the bias caused by different surface types is opposite in the 4K and 6K intervals, which is worth mentioning. An analogous behavior is observed for the SLS fit although it is more sensitive to variations in the background.

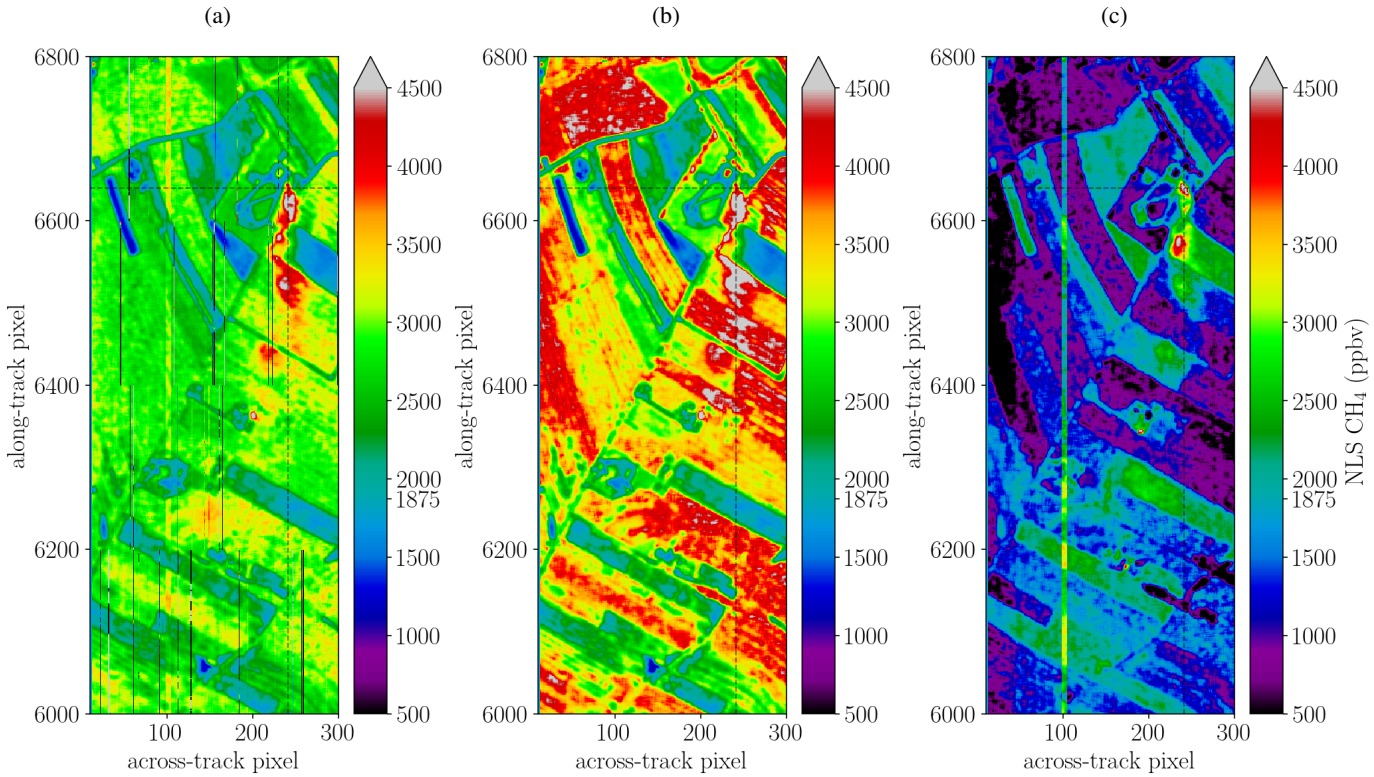

Figure 6. Methane enhancements for 3×3 spatially averaged HySpex observations in the **(a)** multi-interval fit (combining 4K and 6K ranges). **(b)** shows the result for the 4150–4900 cm^{-1} (4K) interval, while **(c)** depicts enhancements inferred from the 5700–6300 cm^{-1} (6K) range. Note that the latter two fits suffer from albedo correlations with the target in opposite direction.

The multi-interval retrieval shown in Figure 6a improves the result by reducing albedo-induced variabilities on the target, however the retrieval still suffers from surface-correlated offsets but to a much smaller degree than single-interval fits. The maximum enhancements and plume pattern are similar, but the downwind shape of the plume is better captured (see Table 2).

3.2 GLS fits

Figure 7 displays the retrieved columns using the generalized least squares (GLS) fit from averaged spectra for scene 09 in the 4K and 6K intervals. Compared to other methods, it reduces the correlation between the methane enhancement and surface reflectivity significantly, resulting in a more distinct plume signal and less background clutter.

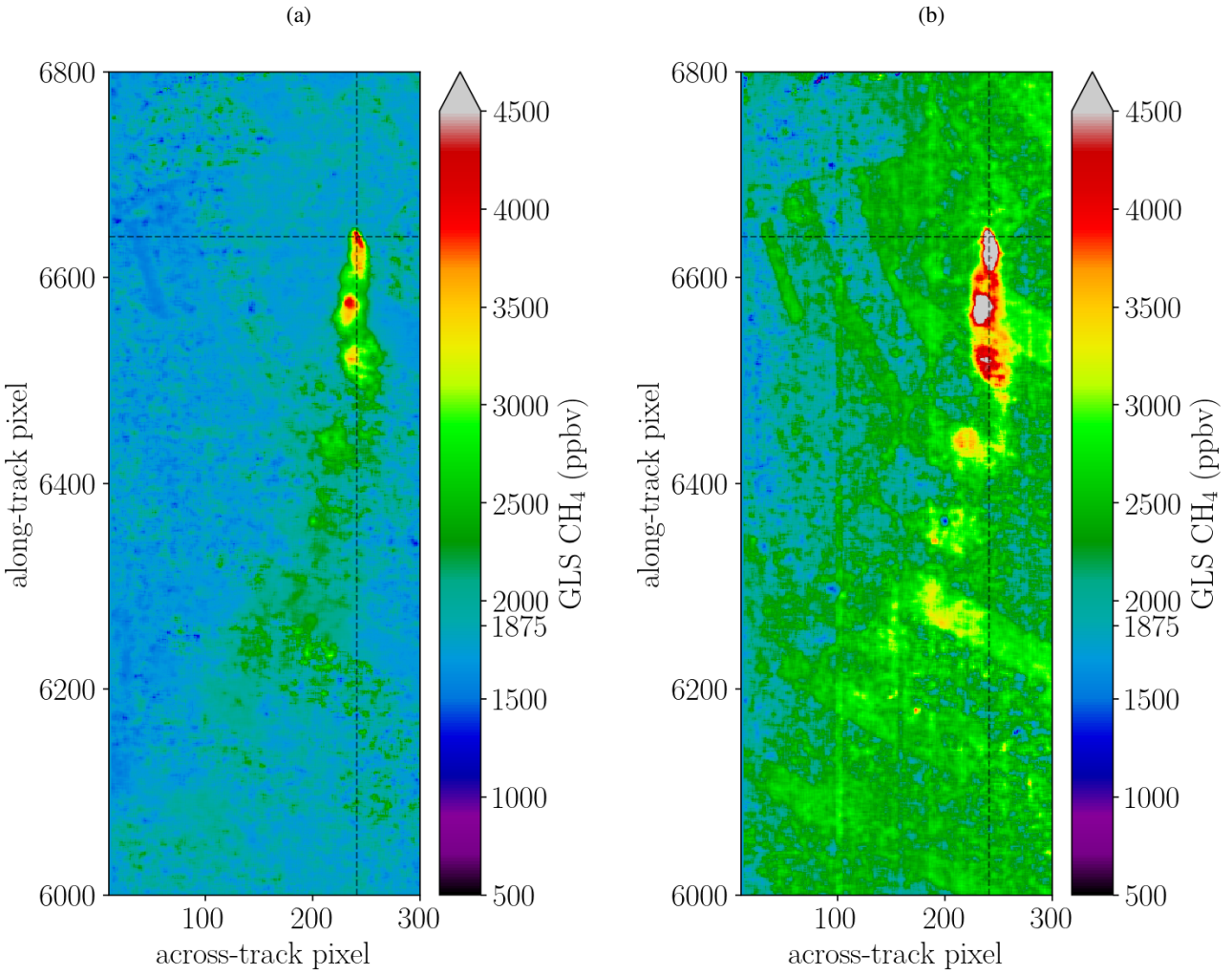

Figure 7. Methane plume depicted for the single window covariance weighted fits for scene 09. The background pixel concentration is rather stable in the 4K interval depicted in **(a)** while there is still some overestimation of CH_4 in the 6K range in **(b)**.

Figure 8 shows the multi-window covariance weighted GLS fits for scene 09 and 11. In both cases the retrieval yields a distinct plume that separates well from background clutter. Figure 8bshows the impact of decreasing ground pixel resolution (from higher altitudes) on the inferred concentrations as enhancements are less pronounced. However, partly this could also be attributed to less emissions since the observation was taken at another point in time. Also winds could have changed as the plume's shape is different compared to scene 09 in Fig. 8a.

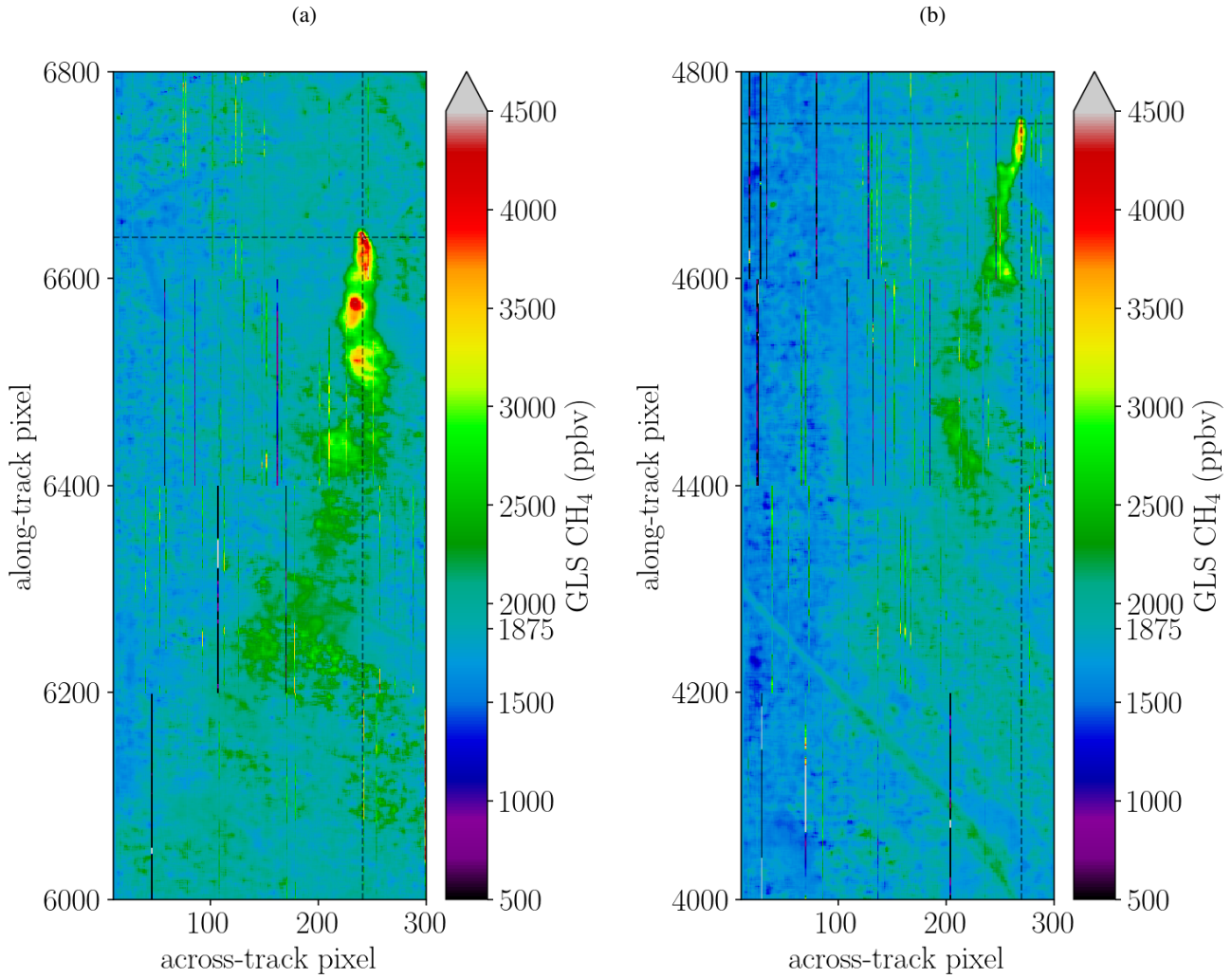

Figure 8. Best results are acquired for GLS setups. **(a)** depicts the enhancements for scene 09 while **(b)** depicts the output for scene 11.The stripe pattern in the along track direction is a multi-window retrieval artefact.

Figure 9 depicts the fits from individual (non-averaged) HySpex spectra for scene 09 and 11 for the GLS multi-window retrieval setup. The single pixel total columns are more affected by retrieval noise caused by the lower signal-to-noise ratio (SNR) which varies significantly over different surface-types. However, the method still identifies elevated methane concentrations and is moreover only minor affected by albedo correlations. Also note that the maximum enhancements are more pronounced, particularly in scene 11 where further degrading ground pixel resolution by spatially averaging apparently has somewhat greater impact on downwind concentrations.

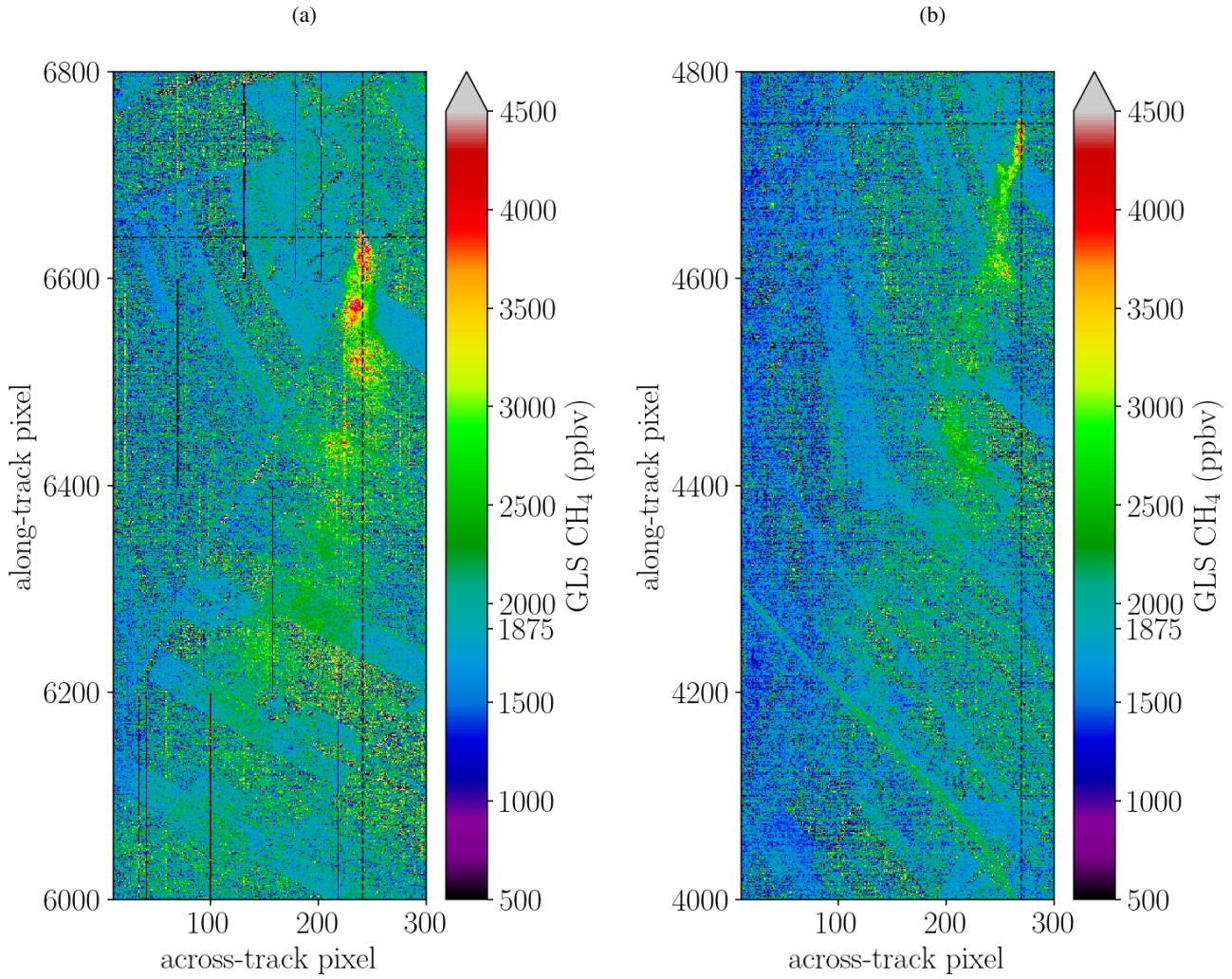

Figure 9. Same as Fig. 8 but for single pixel spectra (not 3×3 averaged). Again **(a)** depicts scene 09 results and **(b)** scene 11.

3.3 MF fits

340 The classical and the albedo normalized matched filter is examined for scene 09. Both variants are able to identify the methane plume but the and as shown in Fig. 10, the cluster-tuning is beneficial in reducing the interference of the plume signal with surface reflectivity.

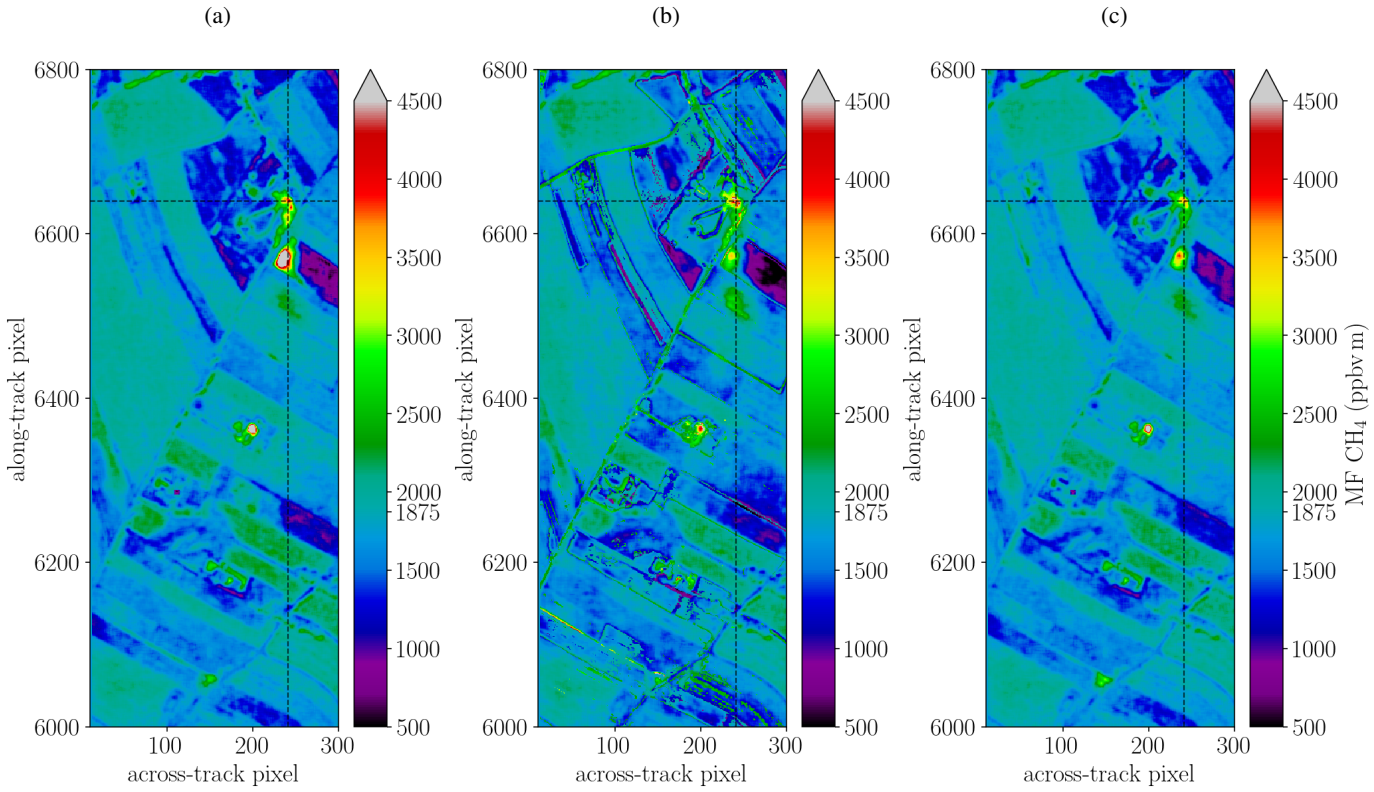

Figure 10. **(a)** Albedo normalized variant of the MF **(b)** the cluster-tuned MF and **(c)** the classical MF fits in the 4K interval (4100-4900 cm^{-1}).

3.4 SVD fits

The SVD-based retrieval method illustrated in Fig. 11 is able to identifying elevated levels CH_4 in the HySpex spectrum. The method yields consistent results for both spectral intervals employing four base vectors and the CH_4 Jacobian for lowest 2km (see Fig. 5). Including more than four base vectors significantly increase the condition number of A as columns five interferes with the methane signal. The albedo normalized MF variant yields somewhat larger CH_4 values depicted in Fig. 10b compared to the classical variant in Fig. 10c. Cluster-tuning also improves the results in Fig. 10a but since the MF already takes background covariance into account the impact is small.

The plume was also identified for the purely 'data-driven' approach, i. e., where the base vector that mimics the CH_4 absorption, i. e., the fifth column in U is used instead of the CH_4 spectrum. This approach does hence not require any forward model and is hence purely data-driven. Cluster-tuning in general improves the fit due to a reduction in variance within each cluster, however, the results become more sensitive to the selected number of base vectors. It was found that within a cluster the number of base vectors required to ensemble A should be reduced.

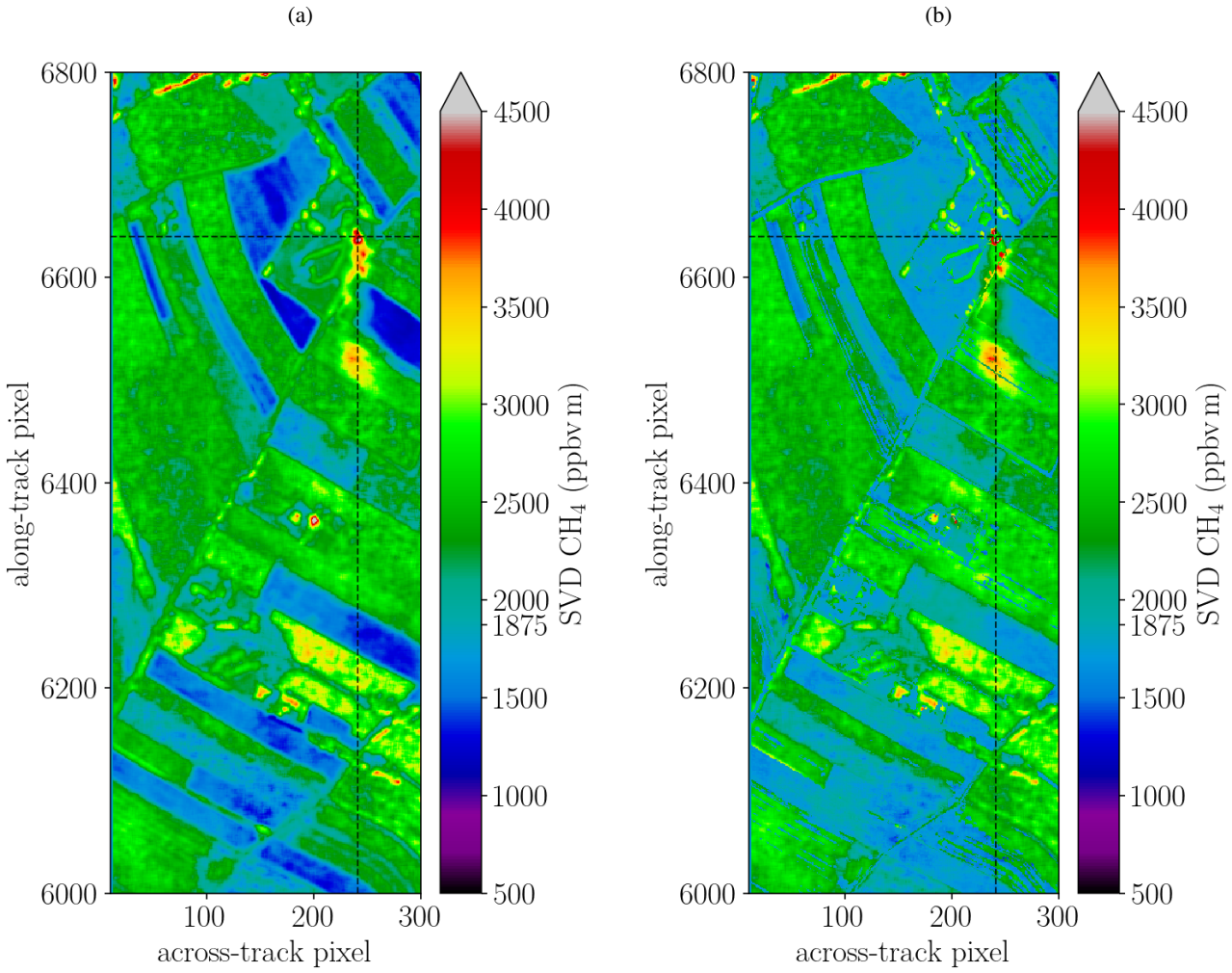

Figure 11. (a) Standard SVD fit and **(b)** background cluster-tuned SVD, both for the 6K spectral range. Three clusters reduce background clutter but suppresses some enhancements close to the source. However, also false positives like the spot around the coordinate (200,6350) are diminished.

3.5 LLS fits

The results for the linearized BIRRA fits are shown in Fig. 12. The method is able to identify CH_4 enhancements, although it differs significantly in the absolute values in the 4K (Fig. 12) and 6K (Fig. 12) spectral range. As pointed out in Sec. 2.4.1, the method is prone to underestimate enhancements. Moreover, the selected weights for the reflectivity coefficients fit were found to impact the CH_4 result. However, for the sake of simplicity and since the optimal selection of weights was not clear at the time of writing no weighting was applied. Its CH_4 results turned out to be sensitive to which deweight the CH_4 impacted pixels. Similar to its nonlinear counterpart (NLS) the fit is also affected by albedo related offsets in opposite directions in the two intervals. However, relative enhancements between plume and background values are rather similar.

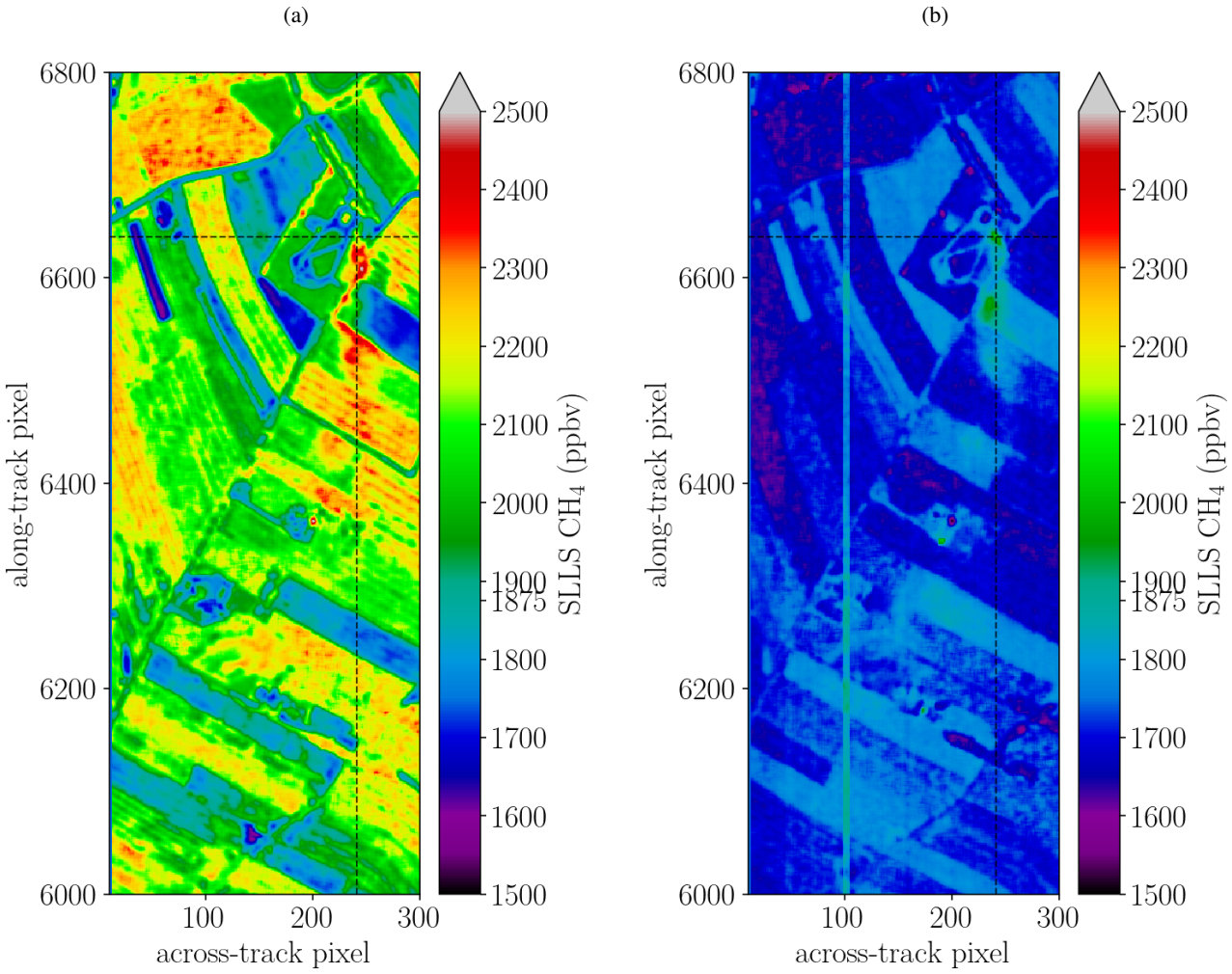

Figure 12. CH_4 enhancements for scene 09 estimated with the linear forward model setup. The results in Fig. **(a)** show the results for the 4K spectral window while Fig. **(b)** shows 6K outcome. In the latter method, the methane enhancements are less pronounced, but the reflectivity related bias is also smaller.

3.6 SSD fits

In Fig. 13 results for the SSD method are shown. A second order polynomial is fitted in Fig. 13a while a constant is used in Fig. 13b. The result show that relative variations are more pronounced in the zero-order fit while the higher order fit better captures the downwind plume by suppressing background clutter.

It is important to note that the method yields better results for the 6K absorption since the 4K absorption features are distributed over a larger spectral range which causes more uncertainty in the out-of-band polynomial fit since many pixels need to be omitted.

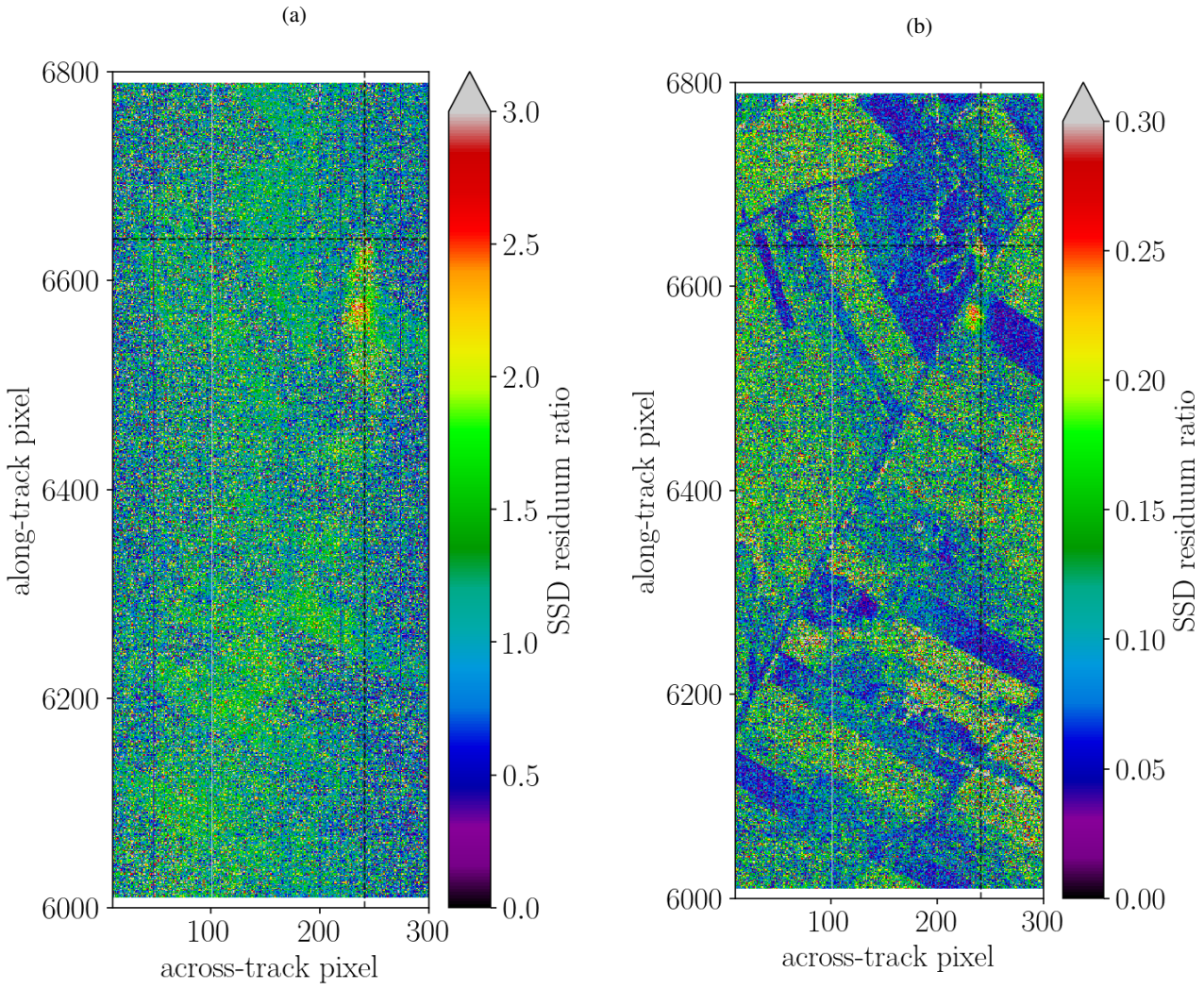

Figure 13. The ratio of the spectral residuals in the 6K range for the in- and out-band pixel are depicted. In **(a)** the in-band residuals were computed towards a quadratic polynomial while in **(b)** a constant was used.

3.7 Statistical significance of results

In order to provide a more quantitative measure on the quality and confidence of the fits a Student's t-test was applied to the results. The test helps to measure how well the plume is represented with respect to the background for a given retrieval setup. This is accomplished by testing for pixels that contradict the null hypothesis (background pixel) and hence should belong to the plume.

The method assumes that the CH_4 background samples are normal distributed with equal variance, and that they are independent (Bruce et al., 2020). The null hypothesis was rejected for significance levels 0.01 which can be considered a strong

evidence against the null hypothesis. Although some fit results may ask for a tighter significance level in the t-test to isolate the plume and get rid of most outliers, for the sake of comparison 0.01 is used throughout this study.

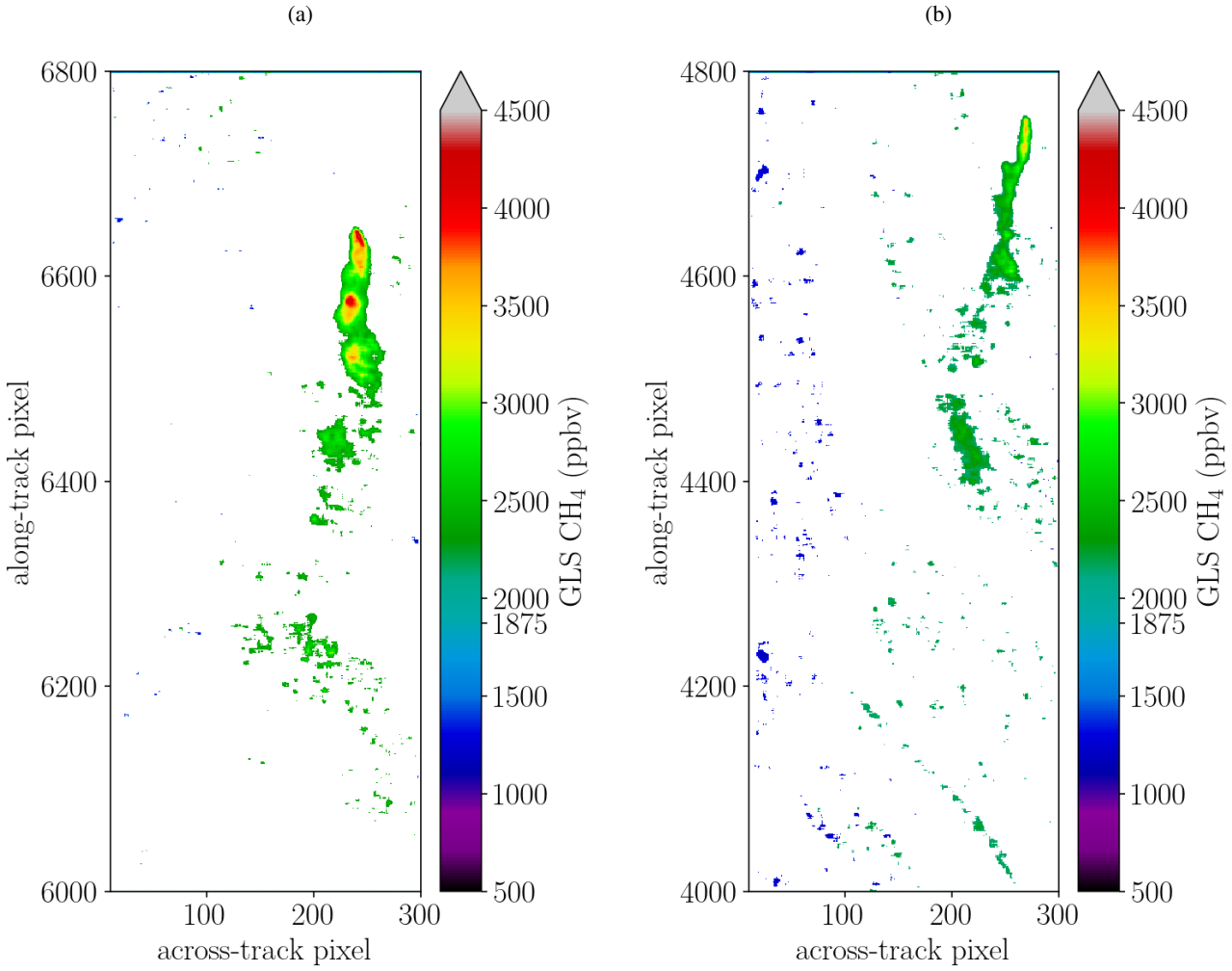

Figure 14. Plume pixels according to the Student's t-test for the nonlinear multi-window GLS fit. **(a)** Shows scene 09 while **(b)** displays scene 11.

Figure 14 depicts the result of the t-test applied to the retrieval output for scene 09 and 11 from the covariance weighted nonlinear solver (GLS) in the 4K range. The plume is well pronounced and the test is able to isolated enhanced CH_4 values from the background. In particular the higher ground-resolution scene 09 shows almost no outliers at the selected significance level meaning that the depicted values occur only in $\leq 1\,\%$ of the cases given the null hypothesis (background methane concentrations) is true. Moreover, finding such extreme values by chance in such a pattern is even more likely and hence the result gives confidence that the is is a methane plume originating at the source that is transported downwind.

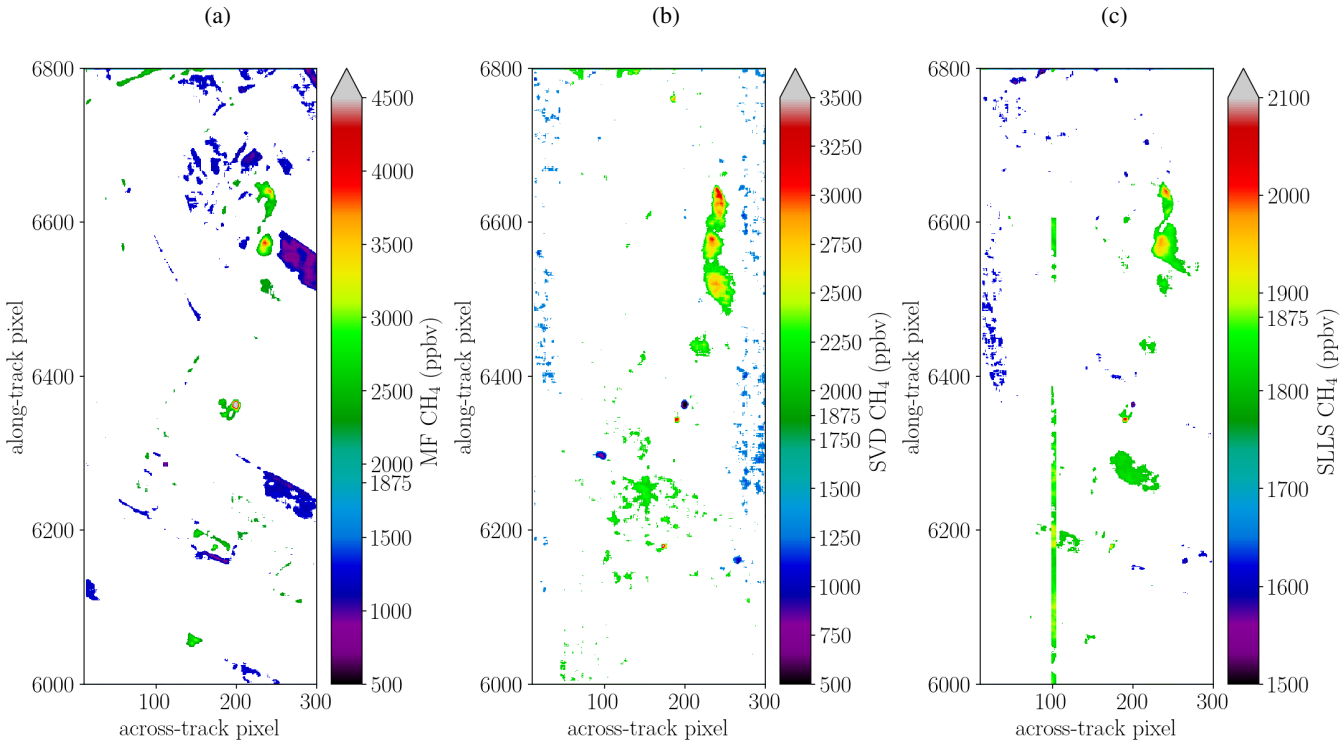

Figure 15. Plume pixels identified by the t-test in scene 09 for the different linear schemes. Note that the color scale was adapted. **(a)** Classical MF output from the 4K range, **(b)** displays plume pixels accoding to the SVD method in the 6K interval, and **(c)** presents the SLLS fit in 6K.

The Student's t-test was also applied to the linear solvers and the results are shown in Fig. 15. The test was performed with the same significance levels as above. Each of the linear methods provide enough pixels within the confident range to isolate the plume pixels. While MF provides most accurate enhancement values with respect to the nonlinear solver in Fig 14 the SVD better captures the downwind plume, however, peak enhancements are $\approx 30\,\%$ lower. The LLS method does capture the downwind plume but is much less sensitive to enhancement as it significantly underestimates these.

3.8 Errors and correlations

In general the retrieval's fit quality is assessed with respect to the discrepancy between the measurement $\boldsymbol{y}$ and the converged spectrum $\boldsymbol{I}$ according to $\sigma = ||\boldsymbol{y} - \boldsymbol{I}(\hat{\boldsymbol{x}})||$, also known as the residual norm. In order to get the uncertainties (variance) in the estimates of the model parameters for a particular fit, the residual norm is multiplied by the retrieval error covariance matrix

$$\boldsymbol{V} = \frac{\sigma^2}{M-N}\,(\mathsf{J}^{\mathrm{T}}\,\mathsf{J})^{-1} \quad \text{with} \quad \hat{\boldsymbol{x}}_i \pm \sqrt{\boldsymbol{V}_{\boldsymbol{ii}}}\,, \tag{19}$$

representing the standard error for the fitted state vector $\hat{\boldsymbol{x}}$ and J the Jacobi matrix.

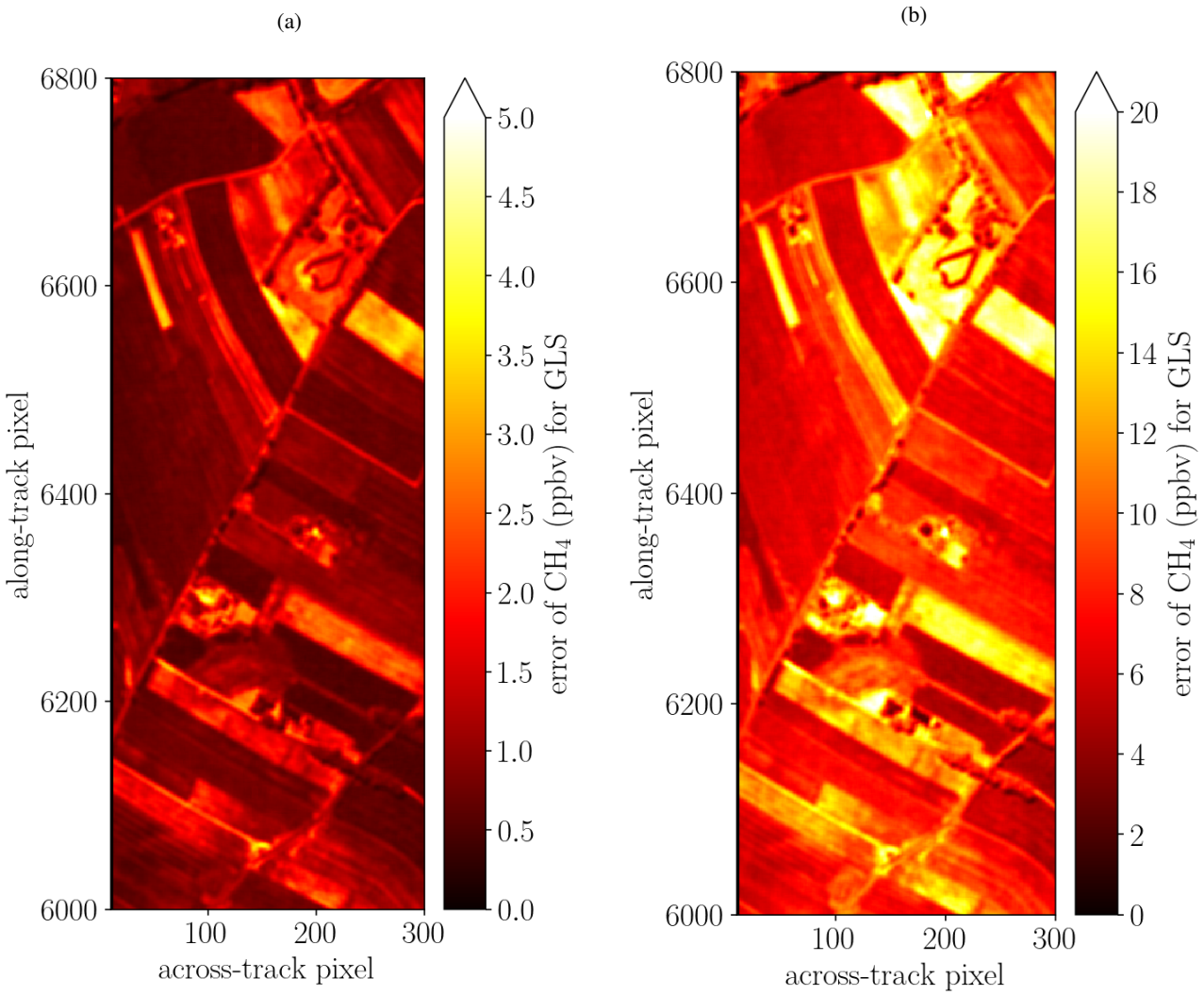

Figure 16. Uncertainties in the estimated CH_4 according to Eq. 19 for the covariance weighted fit in the **(a)** 4K and **(b)** 6K spectral windows. The 6K range shows larger errors as it contains less than half the number of pixels than the 4K window. Beside the higher variances also the bad pixel close to methane lines depicted in Fig. 2 is also likely to increase the spectral residuum norm.

The errors of the individual state vector parameters are represented in the square root of the diagonal elements of $\boldsymbol{V}$. The standard error $\sqrt{\boldsymbol{V_{11}}}$ for the CH_4 scaling factor is shown inf Fig. 16. The uncertainty varies with different surface types which is a product of errors induced by correlation and the spectral residual. A different way to evaluate the quality of the retrieval for a scene is to estimate the fit error from the variability of pixels identified as background by the t-test. This method calculates a score by comparing the means of pixels from the target area and the background area, and dividing this by the standard deviation of the background. These values are also obtainable for all the linear fit variants.

Table 2. Mean and standard error for the background pixels of the t-test. Relating the standard error to the mean is a good indication on the accuracy and precision of a method.

			Background pixels	
Nonlinear Solvers	Window	Score	mean	std. dev.
GLS	4K	5.34	1832	± 150
GLS	6K	4.94	2051	± 122
GLS	4K6K	4.57	1926	± 170
SLS	4K	3.05	3278	± 673
SLS	6K	2.22	1320	± 537
SLS	4K6K	2.94	3085	± 577
NLS	4K	3.05	3247	± 251
NLS	6K	2.21	1369	± 199
NLS	4K6K	3.40	2840	± 244

Tables 2 and 3 present the findings of this analysis for the nonlinear and linear solvers, respectively. The analysis shows that the GLS fit performs best and that SLS and NLS yield similar results while the MF scores highest amongst the linear solvers. In accordance with Fig. 16 fits in the the 4K window score higher, compared to the 6K. Note that the less sensitive the retrieval is to CH_4 enhancements the less variations will be observed in the background. Therefore, the standard deviation in the last column should not be overemphasized in the evaluation of the setups.

Table 3. Same as Table 2 but for the linear retrieval setups.

			Background pixels	
Linear Solvers	Window	Score	mean	std. dev.
MF	4K	4.22	1778	± 208
MF	6K	3.20	1775	± 217
SVD	4K	3.23	2237	± 383
SVD	6K	3.18	1700	± 157
SLLS	4K	2.72	2069	± 140
SLLS	6K	2.71	1713	± 145

Figure 17 shows the correlation matrix of the retrieval outputs for the various solvers and spectral intervals. It reveals that most solvers have rather good correlations with the GLS solvers (sort of benchmark), particularly in the 4K and 4K6K spectral ranges. Moreover, the GLS, MF and SVD show blocks of high correlation. Blue colors indicate that inferred concentrations tend to move in opposite directions which is the case for example in the single window NLS fits in Fig. 6.

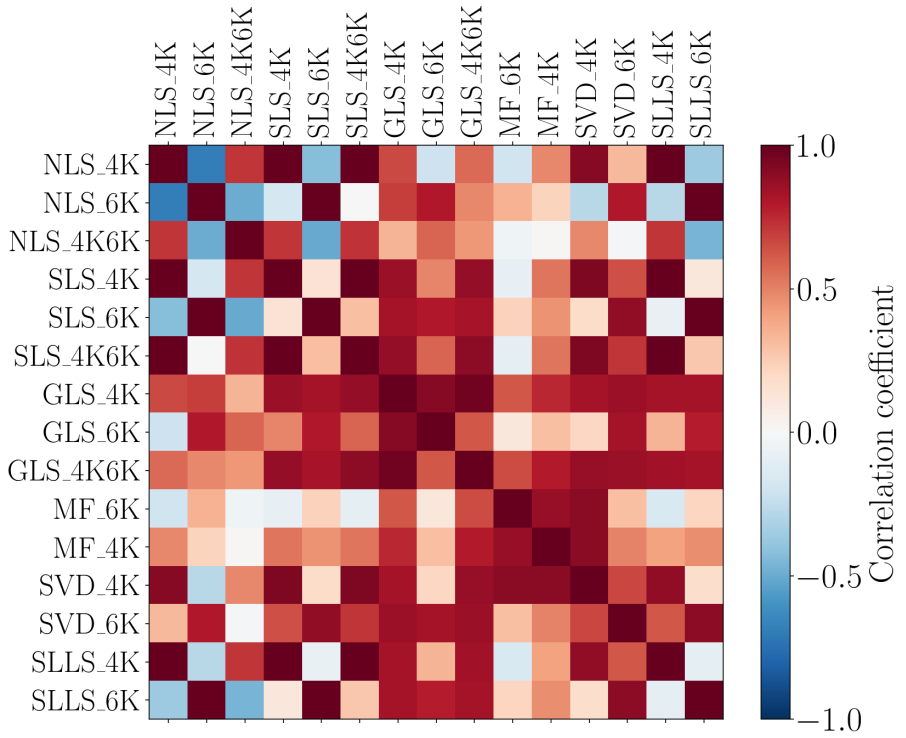

Figure 17. Pearson correlation coefficients for inferred methane from scene 09 for the nonlinear and linear solvers in the two examined spectral intervals.

4 Discussions

This study found that the BIRRA based nonlinear methods which utilize background pixel covariance statistics (GLS) are able to quantify CH_4 concentrations with good accuracy and precision. On the other hand, the unweighted BIRRA suffers from degeneracies between the surface reflectivity and the broad band molecular absorption signal. It was found that the separation of linear (reflectivity coefficients) and nonlinear (target) parameters in the SLS fit does not mitigate the problem of correlation between these quantities but only the inclusion of the background covariance significantly reduces surface reflectance depending biases.

In accordance with Guanter et al. (2021) surface brightness and homogeneity were found to be important factors in detecting and quantifying methane plumes. The issue of different surface types and their impact on the uncertainty of the CH_4 enhancement was also addressed by Borchardt et al. (2021). In accordance with our results the authors noted that retrieval noise can vary significantly depending on surface type, and that different retrieval schemes can yield disparate total column values (see Fig. 9). For example, they found that paved concrete induces a positive bias while barbed goatgrass leads to a underestimation of enhancements and hence the total columns.

In order to scan for potential CH_4 leakages on large datasets with millions of pixels, linear solvers such as the SVD, MF or LLS are more appropriate due to their significantly better speed performance. While the iterative setups require roughly one second per fit the linear methods are two, up to three orders of magnitude faster. In particular the SVD and MF solvers yield enhancements that agree well with the more sophisticated nonlinear BIRRA method although their sensitivity and accuracy is lower which in some cases and hampers the ability to detect downwind patterns. Although the SVD method does not explicitly incorporate a covariance matrix it is important to note that the singular vectors are generated from assumed background pixels, hence the solver takes background statistics into account and is considered an equivalent alternative to the MF approach. Both methods are sensitive to the selection of the background and has significant impact on the retrieval result (Thorpe et al., 2014; Foote et al., 2020).

The simple linearization of the BIRRA forward model lacks background covariance information and hence the fit suffers from albedo correlations similar to its nonlinear counterparts (NLS and SLS). Moreover, the fit significantly underestimates enhancements although it is able to capture parts of the pattern. For the rather simple SSD method polynomials up to second order were able to capture the enhanced methane signal while the selection of an adequate polynomial is depending on the width of the spectral interval and its surface reflectivity. Note that it is not designed to quantify methane but only for (tactical onboard) detection.

As mentioned by other authors before (e. g. Thompson et al. 2015) linear methods should be regarded as a complement to other more complete retrieval algorithms. While linear methods are well-suited to survey vast datasets and pinpoint potential sources, the iterative BIRRA solvers are adequate to quantify enhanced concentrations at known locations as the slower speed is not of much concern for some thousands of observations.

Cluster-tuned linear retrieval setups can help to mitigate background clutter and surface reflectivity induced biases (Nesme et al., 2020), however, incorporation of an adequately compiled background covariance matrix into the fitting scheme was found to be more effective. It was also found that allocating the right cluster for the pixel to be retrieved is crucial in order for the method to improve results as otherwise inaccurate background statistics are used for the fit. Nonetheless, cluster-tuning can be a beneficial preprocessing step as it e. g. allows to potentially reduce the base vectors per cluster in the SVD method since background variability is reduced and fewer base vectors are sufficient to model the background spectrum. However, note that in this case a separate model matrix A needs to be compiled for each cluster.

5 Conclusions

The study examines the feasibility of methane retrievals from hyperspectral imaging observations using various retrieval methods. It was found that localized CH_4 enhancements close to the ground can be quantified from HySpex airborne observations. The generalized covariance weighted BIRRA retrieval is well-suited for investigating potential methane emissions. The statement is underpinned by the relatively low background variations and distinct CH_4 enhancement pattern in the surface-albedo covariance weighted BIRRA fits in, e. g., Fig. 8 and Table 2.

The BIRRA NLS and SLS fits were found to be sensitive to spectral variations in the albedo, leading to surface-type dependent biases that were reported in previous studies utilizing data from hyperspectral sensors. This effect was more pronounced for single spectral intervals but less evident when multiple intervals were used for the fit, such as combining 4K and 6K.

The linear estimators proved to be highly efficient, making them suitable for near real-time processing of large hyperspectral datasets. The well-established MF method for hyperspectral data produced results that agree well with the BIRRA inferred enhancements. The SVD method yields similar enhancements and is able to capture most parts of the downwind plume with great statistical confidence. While also the LLS method is able to capture some of the enhanced plume pixels, it is much less sensitive. For detection purposes the SSD was found to be a useful tool.

In conclusion, covariance weighted methods are able to quantify methane enhancements om hyperspectral SWIR observations at high spatial resolution with good accuracy. The weighted nonlinear methods are more precise and are better suited to capture the downwind plume which is essential for emission estimates. Considering the significant speedup and reasonable accuracy of the linear methods MF and SVD, both constitute a valueable tool in examining plumes on vast datasets.

The methods are applicable to other airborne as well as space borne sensors and this should be considered as a next step. As a final note, the new Python version of the BIRRA code used in this study, based on Py4CAtS as its forward model, turned out to be a flexible toolbox for prototyping.

Code availability. Parts of the code are published via the Py4CAtS software suite (see Schreier et al. (2019))

Data availability. On request

Author contributions. Philipp Hochstaffl (PH) developed and implemented the retrieval setups and analysis tools and wrote the manuscript. Franz Schreier (FS) originally designed and developed the software package Py4CAtS and supported the data evaluation. Claas Köhler (CK) conceived the experimental setup and conducted the data acquisition of the airborne measurements. Andreas Baumgartner (AB) performed the instrument calibration and Level 0-1 processing. CK, AB contributed the experimental setup to the manuscript. Daniele Cerra (DC) gave valuable advice for the cluster-tuning approach and provided spectral unmixing data for the verification of the SVD and MF results. All authors reviewed the manuscript.

Competing interests. The authors declare that they have no conflict of interest.

Acknowledgements. We thank Thomas Trautmann and Peter Haschberger for valuable criticism of the manuscript. Furthermore we thank Konstantin Gerilowski for initiating coorperation with the CoMet campaign and Andreas Fix as the campaign leader for the support and coordination.

References

Hochstaffl, P.: Trace Gas Concentration Retrieval from Short-Wave Infrared Nadir Sounding Spaceborne Spectrometers, Ph.D. thesis, Ludwig-Maximilians-Universität München, 2022.

Hochstaffl, P., Baumgartner, A., Slijkhuis, S., Lichtenberg, G., Koehler, C. H., Schreier, F., Roiger, A., Feist, D. G., Marshall, J., Butz, A., and Trautmann, T.: CO2Image Retrieval Studies and Performance Analysis, Tech. Rep. EGU23-15635, Copernicus Meetings, https://doi.org/10.5194/egusphere-egu23-15635, 2023.

Rast, M., Nieke, J., Adams, J., Isola, C., and Gascon, F.: Copernicus Hyperspectral Imaging Mission for the Environment (Chime), in: 2021 IEEE International Geoscience and Remote Sensing Symposium IGARSS, pp. 108–111, https://doi.org/10.1109/IGARSS47720.2021.9553319, 2021.

Duren, R. M., Thorpe, A. K., Foster, K. T., Rafiq, T., Hopkins, F. M., Yadav, V., Bue, B. D., Thompson, D. R., Conley, S., Colombi, N. K., Frankenberg, C., McCubbin, I. B., Eastwood, M. L., Falk, M., Herner, J. D., Croes, B. E., Green, R. O., and Miller, C. E.: California's Methane Super-Emitters, Nature, 575, 180–184, https://doi.org/10.1038/s41586-019-1720-3, 2019.

Schreier, F., Gimeno García, S., Milz, M., Kottayil, A., Höpfner, M., von Clarmann, T., and Stiller, G.: Intercomparison of Three Microwave/Infrared High Resolution Line-by-Line Radiative Transfer Codes, in: Radiation Processes in the Atmosphere and Ocean (IRS2012): Proceedings of the International Radiation Symposium (IRC/IAMAS), edited by Cahalan, R. F. and Fischer, J., vol. 1531 of *AIP Conference Proceedings*, pp. 119–122, https://doi.org/10.1063/1.4804722, 2013.

Foote, M. D., Dennison, P. E., Thorpe, A. K., Thompson, D. R., Jongaramrungruang, S., Frankenberg, C., and Joshi, S. C.: Fast and Accurate Retrieval of Methane Concentration From Imaging Spectrometer Data Using Sparsity Prior, IEEE Trans. Geosci. Remote Sens., 58, 6480–6492, https://doi.org/10.1109/TGRS.2020.2976888, 2020.

Ayasse, A. K., Thorpe, A. K., Roberts, D. A., Funk, C. C., Dennison, P. E., Frankenberg, C., Steffke, A., and Aubrey, A. D.: Evaluating the Effects of Surface Properties on Methane Retrievals Using a Synthetic Airborne Visible/Infrared Imaging Spectrometer next Generation (AVIRIS-NG) Image, Remote Sens., 215, 386–397, https://doi.org/10.1016/j.rse.2018.06.018, 2018.

Anderson, G., Clough, S., Kneizys, F., Chetwynd, J., and Shettle, E.: AFGL atmospheric constituent profiles (0 - 120 km), Tech. Rep. TR-86-0110, AFGL, 1986.

Baumgartner, A.: Traceable imaging spectrometer calibration and transformation of geometric and spectral pixel properties, Ph.D. thesis, https://doi.org/10.48693/38, 2021.

Baumgartner, A. and Köhler, C. H.: Transformation of point spread functions on an individual pixel scale, Optics Express, 28, 38 682–38 697, https://doi.org/10.1364/oe.409626, tex.date_added: Tue Dec 15 16:52:19 2020, 2020.

Borchardt, J., Gerilowski, K., Krautwurst, S., Bovensmann, H., Thorpe, A. K., Thompson, D. R., Frankenberg, C., Miller, C. E., Duren, R. M., and Burrows, J. P.: Detection and quantification of CH_4 plumes using the WFM-DOAS retrieval on AVIRIS-NG hyperspectral data, Atmos. Meas. Tech., 14, 1267–1291, https://doi.org/10.5194/amt-14-1267-2021, 2021.

Bruce, P., Bruce, A., and Gedeck, P.: Practical Statistics for Data Scientists: 50+ Essential Concepts Using R and Python, O'Reilly Media, 2020.

Buchwitz, M., Rozanov, V., and Burrows, J.: A near-infrared optimized DOAS method for the fast global retrieval of atmospheric CH_4, CO, CO_2, H_2O, and N_2O total column amounts from SCIAMACHY Envisat-1 nadir radiances, J. Geophys. Res., 105, 15 231–15 245, https://doi.org/10.1029/2000JD900191, 2000.

Buchwitz, M., de Beek, R., Bramstedt, K., Noël, S., Bovensmann, H., and Burrows, J. P.: Global carbon monoxide as retrieved from SCIAMACHY by WFM-DOAS, Atm. Chem. Phys., 4, 1945–1960, https://doi.org/10.5194/acp-4-1945-2004, 2004.

Buchwitz, M., de Beek, R., Noël, S., Burrows, J. P., Bovensmann, H., Bremer, H., Bergamaschi, P., Körner, S., and Heimann, M.: Carbon monoxide, methane and carbon dioxide columns retrieved from SCIAMACHY by WFM-DOAS: year 2003 initial data set, Atm. Chem. Phys., 5, 3313–3329, https://doi.org/10.5194/acp-5-3313-2005, 2005.

Chabrillat, S., Guanter, L., Segl, K., Foerster, S., Fischer, S., Rossner, G., Schickling, A., LaPorta, L., Honold, H.-P., and Storch, T.: The Enmap German Spaceborne Imaging Spectroscopy Mission: Update and Highlights of Recent Preparatory Activities, in: IGARSS 2020 - 2020 IEEE Intern. Geosci. and Remote Sens. Symposium, pp. 3278–3281, https://doi.org/10.1109/IGARSS39084.2020.9324006, 2020.

De Leeuw, G., Kinne, S., Léon, J.-F., Pelon, J., Rosenfeld, D., Schaap, M., Veefkind, P. J., Veihelmann, B., Winker, D. M., and Von Hoyningen-Huene, W.: Retrieval of Aerosol Properties, in: The Remote Sensing of Tropospheric Composition from Space, edited by John P. Burrows, U. P. and Borrell, P., Phys. of Earth and Space Environ., pp. 259–313, Springer-Verlag, https://doi.org/10.1007/978-3-642-14791-3_6, 2011.

Delahaye, T., Armante, R., Scott, N., Jacquinet-Husson, N., Chédin, A., Crépeau, L., Crevoisier, C., Douet, V., Perrin, A., Barbe, A., Boudon, V., Campargue, A., Coudert, L., Ebert, V., Flaud, J.-M., Gamache, R., Jacquemart, D., Jolly, A., Kwabia Tchana, F., Kyuberis, A., Li, G., Lyulin, O., Manceron, L., Mikhailenko, S., Moazzen-Ahmadi, N., Müller, H., Naumenko, O., Nikitin, A., Perevalov, V., Richard, C., Starikova, E., Tashkun, S., Tyuterev, V., Vander Auwera, J., Vispoel, B., Yachmenev, A., and Yurchenko, S.: The 2020 edition of the GEISA spectroscopic database, J. Mol. Spectrosc., 380, 111 510, https://doi.org/https://doi.org/10.1016/j.jms.2021.111510, 2021.

Frankenberg, C., Platt, U., and Wagner, T.: Retrieval of CO from SCIAMACHY onboard ENVISAT: detection of strongly polluted areas and seasonal patterns in global CO abundances, Atm. Chem. Phys., 5, 1639–1644, https://doi.org/10.5194/acp-5-1639-2005, 2005.

Frankenberg, C., Thorpe, A. K., Thompson, D. R., Hulley, G., Kort, E. A., Vance, N., Borchardt, J., Krings, T., Gerilowski, K., Sweeney, C., Conley, S., Bue, B. D., Aubrey, A. D., Hook, S., and Green, R. O.: Airborne Methane Remote Measurements Reveal Heavy-Tail Flux Distribution in Four Corners Region, Proc. Nat. Academy Sciences, 113, 9734–9739, https://doi.org/10.1073/pnas.1605617113, 2016.

Funk, C., Theiler, J., Roberts, D., and Borel, C.: Clustering to improve matched filter detection of weak gas plumes in hyperspectral thermal imagery, IEEE Transactions on Geoscience and Remote Sensing, 39, 1410–1420, https://doi.org/10.1109/36.934073, 2001.

Gerilowski, K., Tretner, A., Krings, T., Buchwitz, M., Bertagnolio, P. P., Belemezov, F., Erzinger, J., Burrows, J. P., and Bovensmann, H.: MAMAP – a new spectrometer system for column-averaged methane and carbon dioxide observations from aircraft: instrument description and performance analysis, Atmos. Meas. Tech., 4, 215–243, https://doi.org/10.5194/amt-4-215-2011, 2011.

Gimeno García, S., Schreier, F., Lichtenberg, G., and Slijkhuis, S.: Near infrared nadir retrieval of vertical column densities: methodology and application to SCIAMACHY, Atmos. Meas. Tech., 4, 2633–2657, https://doi.org/10.5194/amt-4-2633-2011, 2011.

Golub, G. and Pereyra, V.: Separable nonlinear least squares: the variable projection method and its applications, Inverse Problems, 19, R1–R26, https://doi.org/10.1088/0266-5611/19/2/201, 2003.

Green, R. O., Carrere, V., and Conel, J. E.: Measurement of atmospheric water vapor using the Airborne Visible/Infrared Imaging Spectrometer, in: ASPRS Conference on ImageProcessing, pp. 73–76, 1989.

Green, R. O., Eastwood, M. L., Sarture, C. M., Chrien, T. G., Aronsson, M., Chippendale, B. J., Faust, J. A., Pavri, B. E., Chovit, C. J., Solis, M., Olah, M. R., and Williams, O.: Imaging Spectroscopy and the Airborne Visible/Infrared Imaging Spectrometer (AVIRIS), Remote Sensing of Environment, 65, 227–248, https://doi.org/https://doi.org/10.1016/S0034-4257(98)00064-9, 1998.

Guanter, L., Irakulis-Loitxate, I., Gorroño, J., Sánchez-García, E., Cusworth, D. H., Varon, D. J., Cogliati, S., and Colombo, R.: Mapping methane point emissions with the PRISMA spaceborne imaging spectrometer, Remote Sensing of Environment, 265, 112 671, https://doi.org/https://doi.org/10.1016/j.rse.2021.112671, 2021.

Hansen, P., Pereyra, V., and Scherer, G.: Least Squares Data Fitting with Applications, Johns Hopkins University Press, 2013.

Hochstaffl, P. and Schreier, F.: Impact of Molecular Spectroscopy on Carbon Monoxide Abundances from SCIAMACHY, Remote Sens., 12, 1084, https://doi.org/10.3390/rs12071084, 2020.

Hochstaffl, P., Schreier, F., Lichtenberg, G., and Gimeno García, S.: Validation of Carbon Monoxide Total Column Retrievals from SCIAMACHY Observations with NDACC/TCCON Ground-Based Measurements, Remote Sens., 10, 223, https://doi.org/10.3390/rs10020223, 2018.

Hochstaffl, P., Schreier, F., Birk, M., Wagner, G., Feist, G. D., Notholt, J., Sussmann, R., and Té, Y.: Impact of Molecular Spectroscopy on Carbon Monoxide Abundances from TROPOMI, Remote Sens., 12, 3486, https://doi.org/10.3390/rs12213486, 2020.

Humpage, N., Boesch, H., Palmer, P. I., Vick, A., Parr-Burman, P., Wells, M., Pearson, D., Strachan, J., and Bezawada, N.: GreenHouse gas Observations of the Stratosphere and Troposphere (GHOST): an airborne shortwave-infrared spectrometer for remote sensing of greenhouse gases, Atmos. Meas. Tech., 11, 5199–5222, https://doi.org/10.5194/amt-11-5199-2018, 2018.

(IMF), D. R. S. T. I.: Airborne imaging spectrometer HySpex, Journal of large-scale research facilities, 2, 1–6, https://doi.org/10.17815/jlsrf-2-151, 2016.

Intergovernmental Panel on Climate Change: Climate Change 2013 – The Physical Science Basis: Working Group I Contribution to the Fifth Assessment Report of the Intergovernmental Panel on Climate Change, Cambridge University Press, https://doi.org/10.1017/CBO9781107415324, 2014.

Jervis, D., McKeever, J., Durak, B. O. A., Sloan, J. J., Gains, D., Varon, D. J., Ramier, A., Strupler, M., and Tarrant, E.: The GHGSat-D imaging spectrometer, Atmos. Meas. Tech., 14, 2127–2140, https://doi.org/10.5194/amt-14-2127-2021, 2021.

Kalnay, E., Kanamitsu, M., Kistler, R., Collins, W., Deaven, D., Gandin, L., Iredell, M., Saha, S., White, G., Woollen, J., Zhu, Y., Chelliah, M., Ebisuzaki, W., Higgins, W., Janowiak, J., Mo, K. C., Ropelewski, C., Wang, J., Leetmaa, A., Reynolds, R., Jenne, R., and Joseph, D.: The NCEP/NCAR 40-Year Reanalysis Project, Bull. Am. Met. Soc., 77, 437–472, https://doi.org/10.1175/1520-0477(1996)077<0437:TNYRP>2.0.CO;2, 1996.

Krings, T., Gerilowski, K., Buchwitz, M., Reuter, M., Tretner, A., Erzinger, J., Heinze, D., Pflüger, U., Burrows, J. P., and Bovensmann, H.: MAMAP — a new spectrometer system for column-averaged methane and carbon dioxide observations from aircraft: retrieval algorithm and first inversions for point source emission rates, Atmos. Meas. Tech., 4, 1735–1758, https://doi.org/10.5194/amt-4-1735-2011, 2011.

Kuze, A., Suto, H., Nakajima, M., and Hamazaki, T.: Thermal and near infrared sensor for carbon observation Fourier-transform spectrometer on the Greenhouse Gases Observing Satellite for greenhouse gases monitoring, Appl. Opt., 48, 6716–6733, https://doi.org/10.1364/AO.48.006716, 2009.

Kuze, A., Suto, H., Shiomi, K., Kawakami, S., Tanaka, M., Ueda, Y., Deguchi, A., Yoshida, J., Yamamoto, Y., Kataoka, F., Taylor, T. E., and Buijs, H. L.: Update on GOSAT TANSO-FTS performance, operations, and data products after more than 6 years in space, Atmos. Meas. Tech., 9, 2445–2461, https://doi.org/10.5194/amt-9-2445-2016, 2016.

Lauvaux, T., Giron, C., Mazzolini, M., d'Aspremont, A., Duren, R., Cusworth, D., Shindell, D., and Ciais, P.: Global assessment of oil and gas methane ultra-emitters, Science, 375, 557–561, https://doi.org/10.1126/science.abj4351, 2022.

Lenhard, K., Baumgartner, A., and Schwarzmaier, T.: Independent laboratory characterization of neo HySpex imaging spectrometers VNIR-1600 and SWIR-320m-e, IEEE Transactions on Geoscience and Remote Sensing, 53, 1828–1841, https://doi.org/10.1109/tgrs.2014.2349737, tex.date_added: Fri May 24 16:15:14 2019, 2015.

Liou, K.-N.: An Introduction to Atmospheric Radiation, Academic Press, second edn., 2002.

Lorente, A., Borsdorff, T., Butz, A., Hasekamp, O., aan de Brugh, J., Schneider, A., Wu, L., Hase, F., Kivi, R., Wunch, D., Pollard, D. F., Shiomi, K., Deutscher, N. M., Velazco, V. A., Roehl, C. M., Wennberg, P. O., Warneke, T., and Landgraf, J.: Methane retrieved from TROPOMI: improvement of the data product and validation of the first 2 years of measurements, Atmos. Meas. Tech., 14, 665–684, https://doi.org/10.5194/amt-14-665-2021, 2021.

Luther, A., Kleinschek, R., Scheidweiler, L., Defratyka, S., Stanisavljevic, M., Forstmaier, A., Dandocsi, A., Wolff, S., Dubravica, D., Wildmann, N., Kostinek, J., Jöckel, P., Nickl, A.-L., Klausner, T., Hase, F., Frey, M., Chen, J., Dietrich, F., Necki, J., Swolkień, J., Fix, A., Roiger, A., and Butz, A.: Towards verifying CH_4 emissions from hard coal mines using mobile sun-viewing Fourier transform spectrometry, Atmos. Meas. Tech. Disc., 2019, 1–19, https://doi.org/10.5194/amt-2019-205, 2019.

Luther, A., Kostinek, J., Kleinschek, R., Defratyka, S., Stanisavljević, M., Forstmaier, A., Dandocsi, A., Scheidweiler, L., Dubravica, D., Wildmann, N., Hase, F., Frey, M. M., Chen, J., Dietrich, F., Necki, J., Swolkień, J., Knote, C., Vardag, S. N., Roiger, A., and Butz, A.: Observational constraints on methane emissions from Polish coal mines using a ground-based remote sensing network, Atmospheric Chemistry and Physics, 22, 5859–5876, https://doi.org/10.5194/acp-22-5859-2022, publisher: Copernicus GmbH, 2022.

Masson-Delmotte, V., Zhai, P., Pirani, A., Connors, S., Péan, C., Berger, S., Caud, N., Chen, Y., Goldfarb, L., Gomis, M., Huang, M., Leitzell, K., Lonnoy, E., Matthews, J., Maycock, T., Waterfield, T., Yelekçi, O., Yu, R., and (eds.), B. Z.: Climate Change 2021: The Physical Science Basis. Contribution of Working Group I to the Sixth Assessment Report of the Intergovernmental Panel on Climate Change, Cambridge University Press, https://doi.org/10.1017/CBO9781107415324, 2021.

Nesme, N., Foucher, P.-Y., and Doz, S.: Detection and quantification of industrial methane plume with the airborne Hyspex-NEO camera and applications to satellite data, in: XXIV ISPRS Congress 2020 edition, vol. XLIII-B3-2020, pp. 821 – 827, Online, France, https://doi.org/10.5194/isprs-archives-xliii-b3-2020-821-2020, 2020.

Nickl, A.-L., Mertens, M., Roiger, A., Fix, A., Amediek, A., Fiehn, A., Gerbig, C., Galkowski, M., Kerkweg, A., Klausner, T., Eckl, M., and Jöckel, P.: Hindcasting and forecasting of regional methane from coal mine emissions in the Upper Silesian Coal Basin using the online nested global regional chemistry–climate model MECO(n) (MESSy v2.53), Geoscientific Model Development, 13, 1925–1943, https://doi.org/10.5194/gmd-13-1925-2020, 2020.

OpenStreetMap contributors: Planet dump retrieved from https://planet.osm.org, https://www.openstreetmap.org, 2022.

Pandya, M. R., Chhabra, A., Pathak, V. N., Trivedi, H., and Chauhan, P.: Mapping of thermal power plant emitted atmospheric carbon dioxide concentration using AVIRIS-NG data and atmospheric radiative transfer model simulations, J. Appl. Remote Sens., 15, https://doi.org/10.1117/1.jrs.15.032204, 2021.

Richter, A.: Satellite remote sensing of tropospheric composition - principles, results, and challenges, EPJ Web of Conferences, 9, 181–189, https://doi.org/10.1051/epjconf/201009014, 2010.

Schneising, O., Buchwitz, M., Burrows, J. P., Bovensmann, H., Bergamaschi, P., and Peters, W.: Three years of greenhouse gas column-averaged dry air mole fractions retrieved from satellite — Part 2: Methane, Atm. Chem. Phys., 9, 443–465, https://doi.org/10.5194/acp-9-443-2009, 2009.

Schreier, F., Gimeno García, S., Hedelt, P., Hess, M., Mendrok, J., Vasquez, M., and Xu, J.: GARLIC – A General Purpose Atmospheric Radiative Transfer Line-by-Line Infrared-Microwave Code: Implementation and Evaluation, J. Quant. Spectrosc. & Radiat. Transfer, 137, 29–50, https://doi.org/10.1016/j.jqsrt.2013.11.018, 2014.

Schreier, F., Gimeno García, S., Hochstaffl, P., and Städt, S.: Py4CAtS — PYthon for Computational ATmospheric Spectroscopy, Atmosphere, 10, 262, https://doi.org/10.3390/atmos10050262, 2019.

Theiler, J. and Foy, B.: Effect of signal contamination in matched-filter detection of the signal on a cluttered background, Geosci. Remote Sens. Letters, 3, 98–102, https://doi.org/10.1109/LGRS.2005.857619, 2006.

Thompson, D. R., Leifer, I., Bovensmann, H., Eastwood, M., Fladeland, M., Frankenberg, C., Gerilowski, K., Green, R. O., Kratwurst, S., Krings, T., Luna, B., and Thorpe, A. K.: Real-time remote detection and measurement for airborne imaging spectroscopy: a case study with methane, Atmos. Meas. Tech., 8, 4383–4397, https://doi.org/10.5194/amt-8-4383-2015, 2015.

Thompson, D. R., Thorpe, A. K., Frankenberg, C., Green, R. O., Duren, R., Guanter, L., Hollstein, A., Middleton, E., Ong, L., and Ungar, S.: Space-based remote imaging spectroscopy of the Aliso Canyon CH4 superemitter, Geophys. Res. Letters, 43, 6571–6578, https://doi.org/https://doi.org/10.1002/2016GL069079, 2016.

Thorndike, R. L.: Who belongs in the family, Psychometrika, pp. 267–276, 1953.

Thorpe, A. K., Roberts, D. A., Bradley, E. S., Funk, C. C., Dennison, P. E., and Leifer, I.: High resolution mapping of methane emissions from marine and terrestrial sources using a Cluster-Tuned Matched Filter technique and imaging spectrometry, Remote Sensing of Environment, 134, 305–318, https://doi.org/https://doi.org/10.1016/j.rse.2013.03.018, 2013.

Thorpe, A. K., Frankenberg, C., and Roberts, D. A.: Retrieval techniques for airborne imaging of methane concentrations using high spatial and moderate spectral resolution: application to AVIRIS, Atmos. Meas. Tech., 7, 491–506, https://doi.org/10.5194/amt-7-491-2014, 2014.

United Nations Framework Convention on Climate: Paris Agreement to the United Nations Framework Convention on Climate Change, https://unfccc.int/files/meetings/paris_nov_2015/application/pdf/paris_agreement_english_.pdf, accessed: 2021-04-01, 2015.

Varon, D. J., McKeever, J., Jervis, D., Maasakkers, J. D., Pandey, S., Houweling, S., Aben, I., Scarpelli, T., and Jacob, D. J.: Satellite Discovery of Anomalously Large Methane Point Sources From Oil/Gas Production, Geophys. Res. Letters, 46, 13 507–13 516, https://doi.org/https://doi.org/10.1029/2019GL083798, 2019.

Veefkind, J., Aben, I., McMullan, K., Förster, H., de Vries, J., Otter, G., Claas, J., Eskes, H., de Haan, J., Kleipool, Q., van Weele, M., Hasekamp, O., Hoogeveen, R., Landgraf, J., Snel, R., Tol, P., Ingmann, P., Voors, R., Kruizinga, B., Vink, R., Visser, H., and Levelt, P.: TROPOMI on the ESA Sentinel-5 Precursor: A GMES mission for global observations of the atmospheric composition for climate, air quality and ozone layer applications, Remote Sensing of Environment, 120, 70 – 83, https://doi.org/10.1016/j.rse.2011.09.027, the Sentinel Missions - New Opportunities for Science, 2012.

Villeneuve, P. V., Fry, H. A., Theiler, J. P., Clodius, W. B., Smith, B. W., and Stocker, A. D.: Improved matched-filter detection techniques, in: Imaging Spectrometry V, edited by Descour, M. R. and Shen, S. S., vol. 3753, pp. 278 – 285, International Society for Optics and Photonics, Proc. SPIE, https://doi.org/10.1117/12.366290, 1999.

Zdunkowski, W., Trautmann, T., and Bott, A.: Radiation in the Atmosphere: A Course in Theoretical Meteorology, Cambridge University Press, 2007.